The Astrophysical Journal, 756:65 (15pp), 2012 September 1 doi:10.1088/0004-637X/756/1/65

COSMIC MICROWAVE BACKGROUND CONSTRAINTS ON THE DURATION AND TIMING OF REIONIZATION FROM THE SOUTH POLE TELESCOPE

O. Zahn[1], C. L. Reichardt[2], L. Shaw[3], A. Lidz[4], K. A. Aird[5], B. A. Benson[6,7], L. E. Bleem[6,8], J. E. Carlstrom[6,7,8,9,10], C. L. Chang[6,7,10], H. M. Cho[11], T. M. Crawford[6,9], A. T. Crites[6,9], T. de Haan[12], M. A. Dobbs[12], O. Doré[13], J. Dudley[12], E. M. George[3], N. W. Halverson[14], G. P. Holder[12], W. L. Holzapfel[3], S. Hoover[6,8], Z. Hou[15], J. D. Hrubes[5], M. Joy[16], R. Keisler[6,8], L. Knox[15], A. T. Lee[3,17], E. M. Leitch[6,9], M. Lueker[13], D. Luong-Van[5], J. J. McMahon[18], J. Mehl[6], S. S. Meyer[6,7,8,9], M. Millea[15], J. J. Mohr[19,20,21], T. E. Montroy[22], T. Natoli[6,8], S. Padin[6,9,13], T. Plagge[6,9], C. Pryke[6,7,9,23], J. E. Ruhl[22], K. K. Schaffer[6,7,24], E. Shirokoff[3], H. G. Spieler[17], Z. Staniszewski[23], A. A. Stark[25], K. Story[6,8], A. van Engelen[12], K. Vanderlinde[12], J. D. Vieira[13], and R. Williamson[6,9]

[1] Berkeley Center for Cosmological Physics, Department of Physics, University of California, and Lawrence Berkeley National Labs, Berkeley, CA 94720, USA; zahn@berkeley.edu
[2] Department of Physics, University of California, Berkeley, CA 94720, USA
[3] Department of Physics, Yale University, P.O. Box 208210, New Haven, CT 06520-8120, USA
[4] Department of Physics and Astronomy, University of Pennsylvania, 209 South 33rd Street, Philadelphia, PA 19104, USA
[5] University of Chicago, 5640 South Ellis Avenue, Chicago, IL 60637, USA
[6] Kavli Institute for Cosmological Physics, University of Chicago, 5640 South Ellis Avenue, Chicago, IL 60637, USA
[7] Enrico Fermi Institute, University of Chicago, 5640 South Ellis Avenue, Chicago, IL 60637, USA
[8] Department of Physics, University of Chicago, 5640 South Ellis Avenue, Chicago, IL 60637, USA
[9] Department of Astronomy and Astrophysics, University of Chicago, 5640 South Ellis Avenue, Chicago, IL 60637, USA
[10] Argonne National Laboratory, 9700 S. Cass Avenue, Argonne, IL 60439, USA
[11] NIST Quantum Devices Group, 325 Broadway Mailcode 817.03, Boulder, CO 80305, USA
[12] Department of Physics, McGill University, 3600 Rue University, Montreal, Quebec H3A 2T8, Canada
[13] California Institute of Technology, MS 249-17, 1216 East California Boulevard, Pasadena, CA 91125, USA
[14] Department of Astrophysical and Planetary Sciences and Department of Physics, University of Colorado, Boulder, CO 80309, USA
[15] Department of Physics, University of California, One Shields Avenue, Davis, CA 95616, USA
[16] Department of Space Science, VP62, NASA Marshall Space Flight Center, Huntsville, AL 35812, USA
[17] Physics Division, Lawrence Berkeley National Laboratory, Berkeley, CA 94720, USA
[18] Department of Physics, University of Michigan, 450 Church Street, Ann Arbor, MI 48109, USA
[19] Department of Physics, Ludwig-Maximilians-Universität, Scheinerstr. 1, D-81679 München, Germany
[20] Excellence Cluster Universe, Boltzmannstr. 2, D-85748 Garching, Germany
[21] Max-Planck-Institut für extraterrestrische Physik, Giessenbachstr. 1, D-85748 Garching, Germany
[22] Physics Department, Center for Education and Research in Cosmology and Astrophysics, Case Western Reserve University, Cleveland, OH 44106, USA
[23] Department of Physics, University of Minnesota, 116 Church Street S.E., Minneapolis, MN 55455, USA
[24] Liberal Arts Department, School of the Art Institute of Chicago, 112 S Michigan Avenue, Chicago, IL 60603, USA
[25] Harvard-Smithsonian Center for Astrophysics, 60 Garden Street, Cambridge, MA 02138, USA
Received 2011 November 23; accepted 2012 June 18; published 2012 August 16

ABSTRACT

The epoch of reionization is a milestone of cosmological structure formation, marking the birth of the first objects massive enough to yield large numbers of ionizing photons. However, the mechanism and timescale of reionization remain largely unknown. Measurements of the cosmic microwave background (CMB) Doppler effect from ionizing bubbles embedded in large-scale velocity streams—known as the patchy kinetic Sunyaev–Zel'dovich (kSZ) effect—can be used to constrain the duration of reionization. When combined with large-scale CMB polarization measurements, the evolution of the ionized fraction, $\bar{x}_e$, can be inferred. Using new multi-frequency data from the South Pole Telescope (SPT), we show that the ionized fraction evolved relatively rapidly. For our basic foreground model, we find the kSZ power sourced by reionization at $\ell = 3000$ to be $D_{3000}^{\rm patchy} \leqslant 2.1\,\mu{\rm K}^2$ at 95% confidence. Using reionization simulations, we translate this to a limit on the duration of reionization of $\Delta z \equiv z_{\bar{x}_e=0.20} - z_{\bar{x}_e=0.99} \leqslant 4.4$ (95% confidence). We find that this constraint depends on assumptions about the angular correlation between the thermal SZ power and the cosmic infrared background (CIB). Introducing the degree of correlation as a free parameter, we find that the limit on kSZ power weakens to $D_{3000}^{\rm patchy} \leqslant 4.9\,\mu{\rm K}^2$, implying $\Delta z \leqslant 7.9$ (95% confidence). We combine the SPT constraint on the duration of reionization with the *Wilkinson Microwave Anisotropy Probe* measurement of the integrated optical depth to probe the cosmic ionization history. We find that reionization ended with 95% confidence at $z > 7.2$ under the assumption of no tSZ–CIB correlation, and $z > 5.8$ when correlations are allowed. Improved constraints from the full SPT data set in conjunction with upcoming *Herschel* and *Planck* data should detect extended reionization at >95% confidence provided $\Delta z \geqslant 2$. These CMB observations complement other observational probes of the epoch of reionization such as the redshifted 21 cm line and narrowband surveys for Lyα-emitting galaxies.

Key words: cosmology: theory – intergalactic medium – large-scale structure of universe

Online-only material: color figures

1. INTRODUCTION

Galaxy-sized dark matter halos first collapse at $z \geqslant 25$. The stars and black holes that form in these halos ultimately ionize and heat the intergalactic medium (IGM). However, exactly when and how this process occurred is unknown.

To date, there have been two primary observational constraints on the reionization era. First, Lyman-α (Lyα) forest absorption spectra toward high-redshift quasars show that the opacity of the IGM to Lyα photons is rapidly increasing at $z \gtrsim 6$ (e.g., Fan et al. 2006b). This increase in opacity has been interpreted as evidence for an increasing neutral hydrogen fraction. However, the interpretation of quasar absorption spectra is hampered by the large cross section for Lyα absorption, which can lead to complete absorption even if the hydrogen ionization fraction is high. At the very least, the amount of transmission in the Lyα forest at $z \lesssim 6$ indicates that the *bulk* of reionization occurred at higher redshifts (McGreer et al. 2011).

Second, *Wilkinson Microwave Anisotropy Probe* (*WMAP*) measurements of the optical depth through large-angle cosmic microwave background (CMB) polarization anisotropy suggest that the redshift of reionization assuming an instantaneous process is $z \simeq 10.6 \pm 1.4$ (Komatsu et al. 2011). CMB polarization measurements offer an integral constraint on the reionization history (Kogut et al. 2003; Page et al. 2007). Therefore, the polarization data are fully consistent with either instantaneous or extended reionization scenarios.

Together, these observations have been interpreted by some as favoring a prolonged reionization epoch ending at $z \simeq 6$ (Miralda-Escude 2003; Cen 2003; Fan et al. 2006b; Bolton & Haehnelt 2007b; Wyithe & Cen 2007). However, the claim that $z \sim 6$ Lyα forest spectra probe the tail end of reionization is somewhat controversial. These data may be consistent with reionization completing at a redshift higher than $z = 6$ (e.g., Oh & Furlanetto 2005; Lidz et al. 2006; Becker et al. 2007; McGreer et al. 2011).

Additional model-dependent constraints on reionization, most of them *upper* limits on the neutral fraction, have been derived by other means: (1) the size of the proximity zone around quasars (Wyithe et al. 2005; Fan et al. 2006b; but see Mesinger et al. 2004; Bolton & Haehnelt 2007a; Lidz et al. 2007; Maselli et al. 2007); (2) the claimed detections of damping wing absorption from neutral IGM in quasar spectra (Mesinger & Haiman 2004, 2007) which were used to place *lower* limits of 20% and 3% on the neutral fraction at $z = 6.3$ (but see Mesinger & Furlanetto 2008a), and more recently a lower limit of 10% at $z = 7.1$ (Mortlock et al. 2011); (3) the *non*-detection of intergalactic damping wing absorption in the spectrum of a gamma-ray burst at $z = 6.3$ (Totani et al. 2006; McQuinn et al. 2008); and (4) the number density and clustering of Lyα emitters (LAEs; Malhotra & Rhoads 2004; Haiman & Cen 2005; Furlanetto et al. 2006; Kashikawa et al. 2006; McQuinn et al. 2007a; Mesinger & Furlanetto 2008b; Ouchi et al. 2010). These constraints will be discussed in more detail in Section 7 and Figure 13.

In this paper, we produce the first constraint on the evolution of the ionized fraction using CMB data. We use new data from the South Pole Telescope (SPT) to constrain the amplitude of the "patchy" kinetic Sunyaev–Zel'dovich (kSZ) signal resulting from inhomogeneous reionization (Knox et al. 1998; Gruzinov & Hu 1998; Santos et al. 2003; Zahn et al. 2005; McQuinn et al. 2005; Iliev et al. 2007b; Fan et al. 2006a). We interpret this signal in the context of reionization models to place the first constraints on the duration of the epoch of reionization using CMB data. A companion paper (Reichardt et al. 2012, hereafter R12) describes the SPT data underlying this measurement in detail. We combine the SPT data with WMAP7 measurements of the integrated opacity due to reionization. The combination makes it possible to constrain the evolution of the ionized fraction, significantly limiting the allowed range of reionization scenarios.

The structure of the paper is as follows. In Section 2, we outline the physics of the kSZ effect from inhomogeneous reionization ("patchy kSZ") and introduce our simulation scheme. We describe the data in Section 3. In Section 4, we set up the model for the CMB and astronomical foregrounds which we fit to the data. In Section 5, we review the constraint on the integrated optical depth by WMAP7 and present the SPT constraints on the amplitude of the patchy kSZ component. In Section 6, we present our constraints on the evolution of the ionized fraction, and forecast future constraints with the SPT, *Planck*, and *Herschel* experiments. We summarize our results and place them in the context of other observations in Section 7.

2. EPOCH OF REIONIZATION AND KINETIC SUNYAEV–ZEL'DOVICH EFFECT

In this section, we review the theory of the kSZ signal, and then introduce the reionization simulations and discuss the kSZ power used to fit to the data.

2.1. CMB Reionization Observables

Scattering of CMB photons into the line of sight introduces temperature anisotropy through the Doppler effect if there are perturbations in the baryon density, $\rho_{\rm b}$, or ionization fraction, x_e. These scatterings slightly change the temperature of the CMB blackbody. The CMB Doppler effect is often called the kSZ effect (Sunyaev & Zel'dovich 1970, 1980) when referring to reionization or the nonlinear regime of structure formation, and the Ostriker–Vishniac effect (Ostriker & Vishniac 1986) when referring to the linear regime, but we will call it the kSZ effect throughout. The total contribution to the temperature anisotropy from a redshift interval $[z_1, z_2]$ is given by

$$\frac{\Delta T_{\rm kSZ}}{T_{\rm CMB}}(\hat{\mathbf{n}}) = \frac{\sigma_T}{c}\int_{z_1}^{z_2} \frac{dx}{dz}\frac{dz}{(1+z)}\bar{n}_e(z)e^{-\tau(z)}\hat{\mathbf{n}}\cdot\mathbf{q}, \qquad (1)$$

where σ_T is the Thomson scattering cross section, dx/dz is the comoving line element, and $\hat{\mathbf{n}}$ is the line-of-sight unit vector. $\bar{n}_e(z)$ is the mean free electron density,

$$\bar{n}_e(z) = \frac{\bar{x}_e(z)\bar{\rho}_b(z)}{\mu_e m_p}, \qquad (2)$$

where $\bar{x}_e(z)$ and $\bar{\rho}_b(z)$ are the mean free electron fraction and mean baryon density of the universe as functions of redshift and $\mu_e m_p$ is the mean mass per electron. We set $\mu_e = 1.22$, appropriate for singly ionized helium. Due to their similar ionization potential, we assume that helium is singly ionized alongside hydrogen, that is, when all hydrogen is ionized and all helium is singly ionized $\bar{x}_e = 1$. Note that $\bar{x}_e = 1.07$ when helium is fully ionized; our model for the post-reionization kSZ signal assumes that this occurs at $z = 3$.

The optical depth, $\tau(z)$, from the observer to redshift z is given by

$$\tau(z) = \sigma_T \int_0^z \frac{\bar{n}_e(z')}{1+z'}\frac{dx}{dz'}dz'. \qquad (3)$$

The *WMAP* large-scale polarization signal constrains the optical depth to the end of recombination, $\tau(z \sim 1000) = 0.088 \pm 0.014$.

Finally, inhomogeneities in the ionization fraction and baryon density enter through

$$\mathbf{q} = (1 + \delta_x)(1 + \delta_b)\mathbf{v}, \quad (4)$$

where $\delta_x = x_e/\bar{x}_e - 1$, $\delta_b = \rho_b/\bar{\rho}_b - 1$, and $\mathbf{v}$ is the bulk motion of free electrons with respect to the CMB.

We discuss the post-reionization kSZ signal in Section 4.1.1. Reionization produces kSZ power primarily through local changes in the ionization fraction. To predict the amplitude of this signal we require a prescription for calculating the evolution of the ionization morphology during the epoch of reionization.

2.2. Efficient Monte Carlo Reionization Simulations

Our ability to infer the properties of the first ionizing sources from observations hinges on the accuracy with which the ionization morphology during reionization can be modeled. A number of groups have developed three-dimensional (3D) radiative transfer codes (e.g., Gnedin 2000; Sokasian et al. 2001; Razoumov et al. 2002; Ciardi et al. 2003; Mellema et al. 2006; McQuinn et al. 2007b; Semelin et al. 2007; Trac & Cen 2007; Altay et al. 2008; Aubert & Teyssier 2008; Finlator et al. 2009; Petkova & Springel 2009). However, the mass resolution and volume requirements for simulations of reionization are daunting. Simulations must resolve the low-mass galaxies (down to the atomic cooling threshold corresponding to a host-halo mass $\sim 10^8\ M_\odot$ at $z \sim 7$–10) that are expected to dominate the ionizing photon budget. They must also be large enough to statistically sample the distribution of ionized regions. These regions can span tens of comoving megaparsecs in size toward the end of reionization (Furlanetto & Oh 2005; Zahn et al. 2005, 2007; Mesinger & Furlanetto 2007; Shin et al. 2008). Recently, some groups have come close to achieving this dynamic range in a single simulation (Iliev et al. 2006; McQuinn et al. 2007b; Trac & Cen 2007; Shin et al. 2008; Trac et al. 2008; Zahn et al. 2011; see Trac & Gnedin 2009 for a recent review).[26]

Given the large uncertainties in the production and escape rates of ionizing photons in high-redshift galaxies (and also in how the photons are absorbed by dense systems), a large parameter space must be explored to interpret observations. These concerns have prompted several groups to develop much more CPU efficient, approximate algorithms (Furlanetto et al. 2004; Zahn et al. 2005, 2007, 2011; Mesinger & Furlanetto 2007; Geil & Wyithe 2008; Alvarez et al. 2009; Choudhury et al. 2009; Thomas et al. 2009). The basic idea is that semi-analytic models can be applied in a Monte Carlo fashion to large-scale realizations of the density and velocity fields. The resulting complex reionization morphology can be compared side by side with simulations based on the same initial conditions combined with the same source and sink prescriptions. We use a modification of the Zahn et al. (2011) model to set up our reionization parameter space.[27]

[26] Note, however, that Lyman limit systems, which can dominate the absorption of ionizing photons (see, for example, the Appendix of Furlanetto & Oh 2005), are still too small to be resolved by state-of-the-art reionization simulations, and are typically included via analytic prescriptions (e.g., Furlanetto & Oh 2005; McQuinn et al. 2007b; Choudhury et al. 2009; Crociani et al. 2010).

[27] The reason we do not use purely analytic models is that they have difficulties describing the partial overlap stage of merging ionized regions (e.g., McQuinn et al. 2005).

The model associates ionized regions with the ionizing sources they contain. The size distribution of ionized regions is related to the halo mass function through the ansatz, $M_{\rm ion} = \zeta M_{\rm gal}$. $M_{\rm gal}$ is the mass in collapsed objects. ζ is the efficiency factor for ionization, and can be decomposed as $\zeta = f_{\rm esc} f_* N_{\gamma/b} n_{\rm rec}^{-1}$. Here, $f_{\rm esc}$ is the escape fraction of ionizing photons from the object, f_* is the star formation efficiency, $N_{\gamma/b}$ is the number of ionizing photons produced per baryon converted into stars, and $n_{\rm rec}$ is the typical number of times a hydrogen atom has recombined. Although the efficiency factor is a rough combination of uncertain source properties, it can encapsulate a wide variety of reionization scenarios.

We calculate $M_{\rm gal}$ according to the extended Press–Schechter model (Bond et al. 1991). In this model, the collapsed fraction (or the fraction of baryons that lie in galaxies) in a region of size r depends on the mean overdensity of that region, $\overline{\delta}(r)$, as

$$f_{\rm coll}(r, M_{\rm min}) = {\rm erfc}\left[\frac{\delta_c(z) - \overline{\delta}(r)}{\sqrt{2[\sigma^2(r_{\rm min}) - \sigma^2(r)]}}\right]. \quad (5)$$

Here, $\delta_c(z)$ is a numerical factor from linear theory equal to 1.686 today, and $\sigma^2(r)$ is the linear-theory rms fluctuation smoothed on scale r. $r_{\rm min}$ is defined as the radius that encloses the mass $M_{\rm min}$ (at average density $\overline{\rho}$) corresponding to a virial temperature of 10^4 K, above which atomic hydrogen line cooling becomes efficient. The redshift dependence of the minimum mass (see Barkana & Loeb 2001) is given in terms of the virial temperature:

$$M_{\rm min} \simeq 10^8 \frac{M_\odot}{h}\left[\frac{T_{\rm vir}}{2\times 10^4\ {\rm K}}\frac{10}{1+z}\right]^{3/2}\left[\frac{\Omega_0}{\Omega_m(z)}\frac{\Delta_c(z)}{18\pi^2}\right]^{-1/2}, \quad (6)$$

with the fitting function $\Delta_c(z) = 18\pi^2 + 82d - 39d^2$ (Bryan & Norman 1998), where $d \equiv \Omega_m(z) - 1$ is evaluated at the collapse redshift. The luminous mass in galaxies required to fully ionize all hydrogen atoms is inversely proportional to the ionizing efficiency, so ionization requires

$$f_{\rm coll} \geqslant \zeta^{-1}. \quad (7)$$

Hence, we can define a barrier $\delta_x(r, z)$ that fluctuations have to cross for their baryonic content to become ionized:

$$\delta(r) \geqslant \delta_x(r, z) \equiv \delta_c(z) - \sqrt{2}{\rm erfc}^{-1}(\zeta^{-1})[\sigma^2(r_{\rm min}) - \sigma^2(r)]^{1/2}. \quad (8)$$

The algorithm then proceeds as follows. For every position, the linear matter overdensity is calculated within a range given by the smoothing kernel (initially set to a large value comparable to the simulation size). Zahn et al. (2011) show that good agreement with radiative transfer simulations is achieved when the smoothing kernel is a top hat in harmonic space. The halo collapse fraction is estimated from this overdensity, and translated with the efficiency factor ζ into an expected number of ionizing photons based on the number of collapsed halos above the atomic cooling threshold mass. The number of ionizing photons is then compared to the number of hydrogen atoms at each point. If there are sufficient ionizing photons, a point is labeled ionized. If not, a smaller radius is set and the algorithm repeated until the resolution of the simulation box is reached.

We optimize the algorithm for mock patchy kSZ spectra at the SPT angular resolution. First, we simulate the density and velocity fields in a rectangular box with a high dynamic range, $1^2 \times 3$ Gpc h^{-1} with $512^2 \times 1536$ volume elements. The

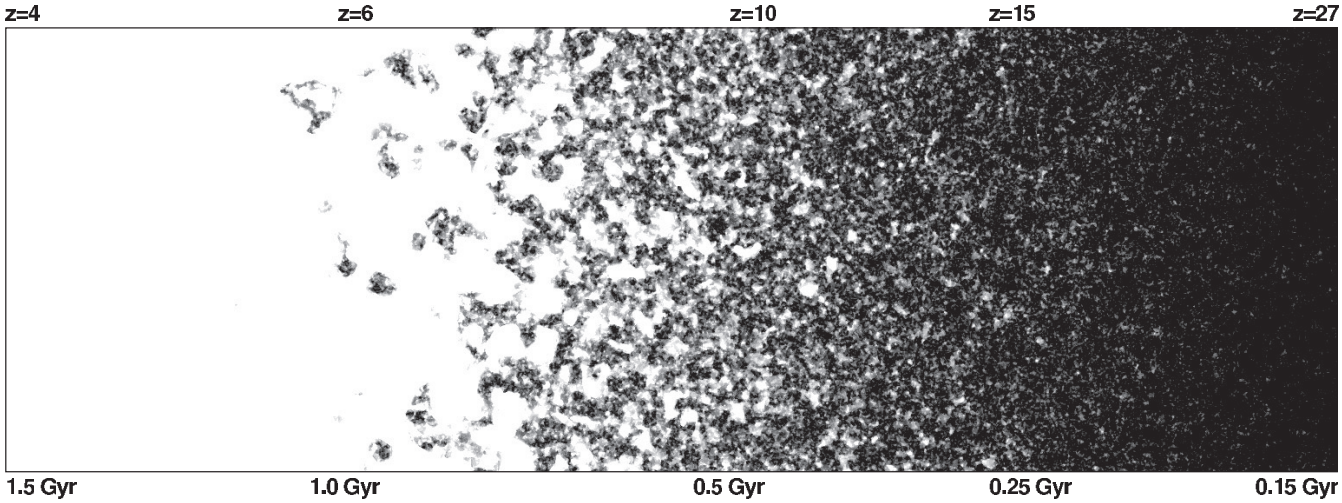

Figure 1. A 20 Mpc h^{-1} deep cut through one of our simulation volumes with dimensions 1×3 Gpc h^{-1}, corresponding to an angular extent of 8.5×8.5 deg at the central $z = 9$ plane, and a redshift coverage from $z \simeq 27$ to $z \simeq 4$. Black means fully neutral and white means fully ionized. Note that this is not a result from fitting to data but a random sample from our simulation database. The ionized fraction in this particular simulation evolves from zero at $z \simeq 20$ to fully ionized at $z = 5.6$.

simulation box subtends 8.5 deg on the sky at the central $z = 9$ plane, yielding arcminute resolution and low sample variance on the scales of interest. Along the z-axis, the comoving distance is translated to redshift. The volume thus extends from $z \simeq 4$ to $z \simeq 27$. The large redshift extent allows us to capture most reasonable reionization scenarios. The densities, velocities, expansion rate, minimum virial mass for star formation, and excursion set barrier (Equation (8)) are adjusted with redshift. The large angular and line-of-sight coverage are important because the ionized regions and large-scale velocity streams that source the kSZ signal appear on scales of tens to hundreds of megaparsecs.

In addition to the global ionization efficiency parameter, ζ, which sets the timing of reionization, it is important to allow for an additional degree of freedom to capture the influence of physical processes that may impact the *duration*, such as feedback effects and recombinations. To do this, we add a "feedback" parameter, α, that makes the effective ionization efficiency an inverse power law of the expected ionization fraction in the absence of feedback, x^*, which is a measure of the ionizing photons available at a given time:[28]

$$\zeta = \zeta_0 \left(\frac{1}{x^*}\right)^{\alpha}, \quad x^* = \zeta_0 f_{\rm coll}(r = \infty, M_{\rm min}). \tag{9}$$

A database of simulated models is set up for $\zeta \in [10, 1000]$ and $\alpha \in [-50, 1]$. This leads to ~10,000 simulations that have reionization durations of $\Delta z \in [0.1, 12]$, and ending redshifts of $z_{\rm end} \in [4, 16]$.[29] Here we have defined $\Delta z = z_{\rm beg} - z_{\rm end}$, $z_{\rm end} = z_{\bar{x}_e=0.99}$, and $z_{\rm beg} = z_{\bar{x}_e=0.20}$. The choice of a relatively large ionization fraction of $\bar{x}_e = 0.20$ for $z_{\rm beg}$ is due to the fact that lower ionized fractions are largely made up of ionized regions too small to be probed by the current SPT data, hence we do not attempt to constrain the reionization state preceding this stage. An example of a 20 Mpc h^{-1} deep projection of an extended reionization simulation with $\zeta = 12$, $\alpha = 0.8$, and $\Delta z \simeq 9$ is shown in Figure 1.

[28] For a constant ionization efficiency ζ ($\alpha = 0$), the simulation predicts a reionization duration of $\Delta z \sim 3$–4, given the definition of Δz below.

[29] Note that the Lyα forest data effectively rule out models that extend past $z_{\rm end} < 5$ (see, e.g., Fan et al. 2006b; McGreer et al. 2011), and we will impose this as a hard prior when deriving reionization constraints in Section 6.

For each reionization simulation, we interpolate rays from constant comoving positions to constant angular positions, produce a map of the kSZ with a size of $\simeq 7 \times 7$ deg, and measure its angular power spectrum. Throughout this paper, power spectra are given in terms of $D_\ell \equiv C_\ell \ell(\ell+1)/2\pi$ (μK^2). For each simulation, we also calculate the total integrated optical depth assuming helium is singly ionized alongside hydrogen and doubly ionized at $z = 3$ (the latter assumption has a negligible influence on the results).

The spatial resolution and box size used lead to convergence of the patchy kSZ amplitude on the relevant angular scale (see the next section). However, the ionized fraction is underestimated during the early stages of reionization, when ionized bubbles smaller than the spatial resolution of the simulation contribute significantly. To correctly predict the duration and integrated optical depth we therefore scale the ionized fraction at each fraction to the analytical value $\zeta f_{\rm coll}(r = \infty, M_{\rm min})$, the mean ionization degree of the universe at that redshift.

In these simulations, we assume a ΛCDM cosmology with $\Omega_c h^2 = 0.111$, $\Omega_b h^2 = 0.0222$, $\Omega_\Lambda = 0.736$, $n_s = 0.96$, $\tau = 0.085$, and $\sigma_8 = 0.8$, consistent with Komatsu et al. (2011). We discuss the cosmological scaling of the kSZ predictions in Section 4.1.1 and the effects of uncertainty in the cosmological parameters in Section 5.2.

2.3. The Kinetic SZ Signal from Reionization

The amplitude and shape of the patchy kSZ power spectrum depend on the redshift evolution of the ionized fraction and the reionization morphology. Here we discuss the dependence of the kSZ power spectrum on the physics of reionization and motivate the template shape used to fit to the SPT data in order to constrain the ionization history.

The reionization model outlined in Section 2.2 has been shown to agree well with full radiative transfer simulations on scales up to 100 Mpc h^{-1} (see, e.g., Zahn et al. 2007, 2011). As a generic consequence of the increase in source collapse fraction with time, the size distribution of ionized regions and volume filling factor evolve more slowly at the beginning of reionization than at the end. Also, the roles of feedback effects and recombinations depend on the degree of ionization. If we instead used a model with a parameterized yet

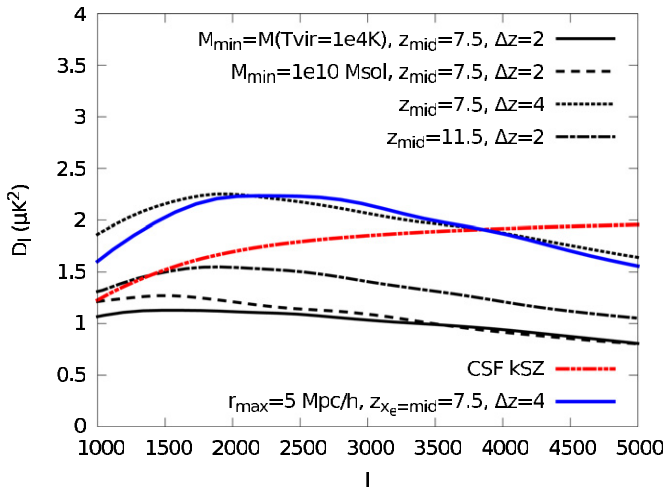

Figure 2. kSZ power spectra due to patchy reionization for different $z_{\rm mid}$, defined by $x_e = 0.5$ (dot-dashed vs. dotted black lines), minimum star-forming mass $M_{\rm min}$ (dashed vs. solid black lines), and maximum ionized bubble scale (blue solid line). The different $M_{\rm min}$ cases are shown at a smaller Δz to allow plotting in the same panel. The blue solid line shows the kSZ power spectrum for a reionization model with $r_{\rm max} = 5$ Mpc h^{-1}. The red, dot-dashed line shows our fiducial homogeneous kSZ template (see Section 4.1.1).

(A color version of this figure is available in the online journal.)

physically unmotivated analytic form of $\bar{x}_e$, the relation between the redshift corresponding to various ionization fractions $z_{\bar{x}_e}$, the kSZ power, and integrated optical depth τ would be different, potentially biasing constraints on $\bar{x}_e$.

Using radiative transfer simulations, it has been found that the size distribution of ionized regions at fixed $\bar{x}_e$ is relatively robust to redshift translations $z_1 \rightarrow z_2$ (e.g., Zahn et al. 2007; McQuinn et al. 2007b). In addition, the angular size corresponding to a given comoving scale varies little across the redshifts of interest. The change in the patchy kSZ power spectrum due to a translation from $z_{\rm mid} \simeq 7.5$ to $z_{\rm mid} \simeq 11.5$, where $z_{\rm mid} \equiv z_{\bar{x}_e=0.5}$, for similar Δz is shown by the black solid and dot-dashed lines in Figure 2. The shapes of both power spectra are very similar, with the main difference being in their normalization. The amplitude is increased in the $z_{\rm mid} \simeq 11.5$ model due to the higher mean density of the universe at higher redshift, which is counteracted somewhat by linear growth of density and velocity fields toward later times.

When moving to higher redshifts, rarer sources have to yield enough ionizing photons. Such sources are more heavily biased, and their lower number density yields larger and more spherical ionized regions (Zahn et al. 2007; McQuinn et al. 2007b). The same is true at low redshifts if feedback effects limit the role of low-mass sources. For instance, low-mass sources might suffer from thermal feedback onto their host galaxies during early stages of reionization (Hultman Kramer et al. 2006; Iliev et al. 2007a). The effect on the patchy kSZ power spectrum of increasing the minimum source mass to $10^{10}\,M_\odot$ (an increase of two orders of magnitude over the fiducial $M_{\rm min}$, discarding >90% of sources, e.g., Trac & Cen 2007) is shown by the black solid and dashed lines in Figure 2. The impact of source bias on the shape of the patchy kSZ template is found to be small compared to our experimental uncertainty.

Furthermore, recombinations in dense systems might effectively stall bubble growth early on in reionization, leading to a slowly percolating web of similarly sized ionized regions (Furlanetto & Oh 2005). To estimate the effect of such a scenario on the kSZ power spectrum, we impose a relatively extreme maximum bubble scale of $r_{\rm max} = 5$ Mpc h^{-1}. The result is shown by the blue solid line in Figure 2. Again, the changes are modest when compared to a model with the same duration but no limit on the bubble scale (dotted curve).

We conclude that the shape of the kSZ power spectrum due to patchy reionization is relatively robust to the effects of redshift translation, feedback, and recombinations. Most importantly for this work, the amplitude is expected to be proportional to the duration of reionization for uncorrelated ionized regions and fixed $z_{\rm mid}$ (e.g., Gruzinov & Hu 1998). If the duration doubles in this Poisson process, there are twice as many independently moving ionized regions along the line of sight, which doubles the power. We find this to be a good approximation to the results from our simulations on the angular scales of interest (compare solid versus dotted lines in Figure 2).

Given the robustness of the *shape* of the patchy kSZ power spectrum to all these changes, we will assume a fixed template shape to derive our reionization results. As base template we choose a model with an efficiency of $\zeta = 20$, making this model extend from $z_{\bar{x}_e=0.2} \simeq 11.0$ to $z_{\bar{x}_e=0.99} \simeq 7.8$; however, as explained above the results are robust to variations in this choice. The base template used to compare to the SPT data was run at eight times higher spatial resolution than the simulations in the database. The resolution of the latter was chosen to lead to convergence at $\ell = 3000$ to allow comparison to the data-derived constraint on the power on that scale; see Section 5.2.

3. DATA

Here we describe the data used in this work, which serve to constrain either the ΛCDM model and primary CMB anisotropy, or the cosmic infrared background (CIB) and the thermal (tSZ) and kinetic (kSZ) Sunyaev–Zel'dovich effects. For the ΛCDM cosmological model, we include measurements of the baryon acoustic oscillation feature from Sloan Digital Sky Survey and 2dFGRS (Percival et al. 2010), a measurement of the Hubble constant from the *Hubble Space Telescope* (Riess et al. 2011), and measurements of the primary CMB from WMAP7 (Larson et al. 2011) and SPT (Keisler et al. 2011). Most importantly for this work, the CMB+BAO+H_0 preferred optical depth is $\tau = 0.085 \pm 0.014$. The optical depth constraint is primarily due to the large-scale polarization and polarization–temperature cross-correlation data from WMAP7.

The above data sets do not constrain the Sunyaev–Zel'dovich effects or CIB, which dominate the anisotropies at arcminute scales and SPT wavelengths. For these small-scale anisotropies, we include new multi-frequency data from the SPT (R12) and the recent *Planck*/HFI CIB bandpowers at 217 GHz (Planck Collaboration 2011). The SPT bandpowers are based on observations at 95, 150, and 220 GHz of 800 deg^2 of sky. From these maps, R12 estimates multi-frequency bandpowers covering angular scales $2000 < \ell < 9400$. The three-frequency SPT bandpowers are used to constrain the CIB, tSZ, and kSZ power spectra. The *Planck*/HFI data aid in constraining the CIB frequency dependence and its angular dependence on large scales.

4. MODEL FITTING

We use Monte Carlo Markov chain (MCMC) techniques to fit the data with a ΛCDM cosmological model including lensed primary CMB anisotropy, tSZ anisotropy, kSZ anisotropy, and foregrounds. The model and parameter fitting is described fully in R12. Here we briefly describe the full model before focusing

on the elements shown by R12 to be important for the kSZ power measurement.

We adopt the standard, six-parameter, spatially flat, ΛCDM cosmological model to predict the primary CMB temperature anisotropy. R12 considers model extensions including running of the spectral index, massive neutrinos, and freedom in the number of neutrino species, finding no effect on the kSZ constraints. R12 also shows that the systematic uncertainty in kSZ power due to uncertainty in the CMB lensing potential is much smaller than the derived kSZ uncertainties.

We include seven free parameters for the small-scale temperature anisotropies from the tSZ and kSZ effects, and the CIB. We also include radio galaxies and galactic cirrus with strong priors as described by R12. Two parameters are the amplitudes of the tSZ and kSZ power spectra; the remaining five parameters describe the CIB model. The chosen tSZ template is the baseline model from Shaw et al. (2010). R12 shows that the resulting kSZ power spectrum results are insensitive to the shape of the tSZ template. The kSZ template and CIB model are critical for the reionization constraints in this work, and will be described next.

4.1. Kinetic Sunyaev–Zel'dovich Effect

We adopt two main templates for the kSZ power spectrum. The first template includes only the contribution from patchy reionization (see Section 2). The second and more realistic template includes roughly equal contributions from the reionization and post-reionization epochs. We henceforth refer to the post-reionization, homogeneously ionized component as the "homogeneous kSZ" signal, and that from reionization as the "patchy kSZ" signal. We discuss the homogeneous kSZ model next.

4.1.1. Homogeneous Kinetic Sunyaev–Zel'dovich Effect

For the homogeneous kSZ signal, we adopt the cooling plus star formation (CSF) model presented by Shaw et al. (2011). This model is constructed by calibrating an analytic model for the homogeneous kSZ power spectrum with a hydrodynamical simulation including metallicity-dependent radiative CSF. Shaw et al. (2011) measured the power spectrum of gas density fluctuations in the simulation over a range of redshifts, and used this to calculate the homogeneous kSZ power spectrum. The approximate scaling for this model with cosmological parameters is given by

$$D_{3000}^{\rm homog} \simeq 1.9\,\mu{\rm K}^2 \left(\frac{h}{0.71}\right)^{1.7} \left(\frac{\sigma_8}{0.80}\right)^{4.5} \left(\frac{\Omega_b}{0.044}\right)^{2.1} \times \left(\frac{\Omega_m}{0.264}\right)^{-0.44} \left(\frac{n_s}{0.96}\right)^{-0.19}. \quad (10)$$

This scaling (but not amplitude) is also a good approximation to the cosmological dependence of the patchy kSZ component. We vary the predicted post-reionization $D_{3000}^{\rm homog}$ with $z_{\rm end}$ when interpreting the results in Section 6. The CSF model kSZ component for $z_{\rm end} = 8$ is shown by the red line in Figure 2. The model utilized here assumes helium is singly ionized between $3 \leqslant z \leqslant z_{\rm end}$ and doubly ionized for $z < 3$.

4.2. Dusty Galaxies (CIB)

The CIB is produced by thermal emission from dusty star-forming galaxies (DSFGs) over a very broad range in redshift (Lagache et al. 2005; Marsden et al. 2009). The dust grains, ranging in size from a few molecules to 0.1 mm, absorb light at wavelengths smaller than their size, and re-radiate it at longer wavelengths. Sufficient absorption occurs to account for roughly equal amounts of energy in the CIB and in the unprocessed starlight that makes up the optical/UV background (Dwek & Arendt 1998; Fixsen et al. 1998).

The power spectrum of these DSFGs will have Poisson and clustered components. Both CIB components have more power than the kSZ power spectrum on the angular scales and photon frequencies of interest (except at 95 GHz where the powers are comparable). The Poisson component shows up as $D_\ell \propto \ell^2$ since the galaxies are small (effectively point sources) compared to the angular scales probed here. We model the clustered component by a power law of the form $D_\ell \propto \ell^{0.8}$, a shape motivated by recent observations (Addison et al. 2012; R12). We have explored allowing freedom in the angular shape via freeing the power-law exponent or adding a linear-theory template, and find that the additional shape parameter increases the kSZ uncertainties by ∼10% without changing the mean.

The frequency dependence of the CIB is a key question for the kSZ measurement. Essentially, the CIB is well measured at ⩾220 GHz by SPT, *Planck*, and other experiments, but the signal to noise falls off toward longer wavelengths. The CIB power at 95 GHz is an extrapolation based on a fit to the modeled frequency dependence. Following previous work, we adopt the phenomenological modified blackbody model:

$$\eta_\nu = \nu^\beta B_\nu(T), \quad (11)$$

where ν is the observing frequency and $B_\nu(T)$ is the blackbody spectrum for temperature T. T and β are free parameters with uniform priors $T \in [5, 35\,K]$ and $\beta \in [0, 2]$. R12 also examined the single-spectral energy distribution (SED) model presented by Hall et al. (2010). The resulting kSZ power upper limits were similar when allowing for the possibility of correlation between the CIB and tSZ and 20% tighter when any correlation was assumed to be negligibly small.

We assume the clustering and Poisson components have the same frequency scaling in this work. Implicitly this is equivalent to assuming that the source populations and redshift distributions are similar. Hall et al. (2010) argued that any difference in the frequency scaling should be small based on CIB simulations. As mentioned in R12, the data have some preference for differing spectral indices when considering the 95–220 GHz alone, however this preference vanishes when *Planck*/HFI 353 GHz data are added.

4.3. Correlation between the tSZ and CIB

An important component of our model is the potential for a spatial correlation between the DSFGs that produce the CIB and the groups and clusters that generate the tSZ power spectrum. At $\ell = 3000$, most of the tSZ power is predicted to originate from clusters of mass greater than $5 \times 10^{13}\,h^{-1}\,M_\odot$ and redshift less than 1.5 (Shaw et al. 2009; Battaglia et al. 2011; Trac et al. 2011). If the galaxies residing in these halos contribute a significant fraction of the CIB power at the SPT frequencies, then the spatial correlation between the tSZ and CIB signal will be non-negligible. Below 220 GHz, the tSZ effect produces temperature decrements; we thus expect an anti-correlation between the CIB and tSZ fluctuations. Note that cross-spectra involving the 220 GHz band—the tSZ null frequency—may still contain power due to tSZ–CIB correlation as the CIB signal couples with the tSZ at the second frequency.

Following R12, we model the contribution of a tSZ–CIB correlation to the measured power spectrum as

$$D^{\mathrm{tSZ-CIB}}_{\ell,\nu_i\nu_j} = \xi_\ell \left[\sqrt{\left(D^{\mathrm{tSZ}}_{\ell,\nu_i\nu_i} D^{\mathrm{CIB}}_{\ell,\nu_j\nu_j}\right)} + \sqrt{\left(D^{\mathrm{tSZ}}_{\ell,\nu_j\nu_j} D^{\mathrm{CIB}}_{\ell,\nu_i\nu_i}\right)} \right]. \quad (12)$$

Here $D^{\mathrm{tSZ-CIB}}_{\ell,\nu_i\nu_j}$ is the power due to correlations, $D^{\mathrm{tSZ}}_{\ell,\nu_i\nu_i}$ is the tSZ power spectrum at frequency i, and $D^{\mathrm{CIB}}_{\ell,\nu_i\nu_i}$ is the sum of the Poisson and clustered CIB components. ξ is the correlation coefficient; we define ξ_{3000} as the amplitude of this correlation at $\ell = 3000$. We consider two templates for the spatial dependence of the correlation, one flat and one rising with ℓ. The reasoning behind these templates is discussed later in this section.

R12 measures the magnitude of the tSZ–CIB correlation by introducing ξ as a free parameter in their model fit to the SPT bandpowers, assuming an ℓ-independent template for $D^{\mathrm{tSZ-CIB}}_{\ell}$. They find $\xi_{3000} = -0.18 \pm 0.12$, consistent with a fraction of the CIB emission being spatially coincident with the tSZ signal. However, George et al. (2011) extrapolate the 24 μm flux of galaxies in their (X-ray-selected) group catalog to 2 mm and find a very small signal. Even allowing for uncertainties in this extrapolation, they conclude that the contamination of DSFGs to the tSZ signal is no more than a few percent. This would imply only a very weak spatial correlation between these signals. A robust measurement of the total DSFG emission in groups and clusters at millimeter/submillimeter wavelengths would place tight observational constraints on ξ_ℓ.

There currently does not exist any published theoretical estimates of the magnitude of the tSZ–CIB correlation. However, we find that the publicly available simulations of Sehgal et al. (2010) predict a large anti-correlation. Taking the cross-spectrum of their simulated CIB-only and tSZ-only maps at 148 GHz, we find $\xi_{3000} = -0.37$.

We make new predictions for the tSZ–CIB correlation by combining the tSZ model of Shaw et al. (2010) with the halo-model-based CIB calculations of Shang et al. (2012). In brief, the Shang et al. (2012) model populates halos and sub-halos with DSFGs utilizing the halo mass function of Tinker et al. (2008) and the sub-halo mass function of Wetzel & White (2010). It is assumed that the relation between galaxy luminosity and sub-halo mass is lognormal, with free parameters for the overall normalization, characteristic mass, and redshift evolution. These parameters are calibrated by comparing the model predictions with the recent *Planck* measurements of the CIB power spectrum (Planck Collaboration 2011). Shang et al. (2012) explore model parameter constraints for various scenarios in which the characteristic dust temperature of DSFGs, the redshift evolution of the sub-halo mass—DSFG luminosity relation, or the shape of their SED are alternatively fixed or allowed to vary. For each of these scenarios (labeled "cases 0–5" in Shang et al. 2012), we calculate the correlation coefficient, ξ.

We find that the predicted value of ξ_{3000} varies between $-0.02 > \xi_{3000} > -0.34$, well within the range found by R12. ξ depends sensitively on the assumed redshift evolution of DSFG luminosity (or equivalently, the evolution of their star formation rate), which always increases toward higher redshift. For models in which the luminosity evolves rapidly, a larger fraction of the CIB power is contributed by high-redshift ($z > 2$) objects and thus the magnitude of ξ decreases.

The ℓ-dependence of ξ also varies between our CIB models. In Figure 3, we plot ξ_ℓ for each of the model cases presented by Shang et al. (2012). The values of ξ_{3000} are given in the caption. The shaded region represents the 1σ and 2σ constraints on ξ obtained by R12. We find a general trend that the correlation coefficient is a stronger function of ℓ for models in which the overall amplitude is closer to zero. This is straightforward to understand; models with a lower value of $|\xi|$ are those for which high-redshift galaxies contribute a larger fraction of the total CIB power. Most of the tSZ–CIB correlation then comes from higher redshift halos which principally contribute to the tSZ power at small scales. Therefore, the correlation coefficient increases with ℓ.

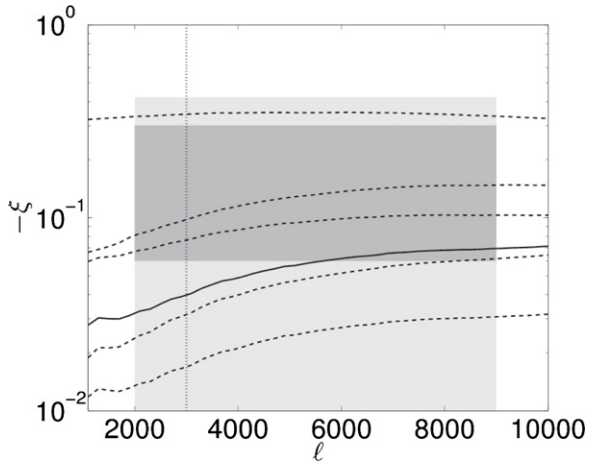

Figure 3. Correlation coefficient ξ calculated for the various CIB model cases presented in Shang et al. (2012). The correlation coefficients at $\ell = 3000$ are (from top to bottom) $\{-0.34, -0.09, -0.07, -0.04, -0.03, -0.02\}$. The slope of the correlation with ℓ becomes steeper as $|\xi|$ decreases. The magnitude of ξ is most sensitive to the redshift evolution of the halo mass–DSFG luminosity relation; a more rapid increase in luminosity with redshift shifts the peak of the CIB to higher redshifts and therefore reduces the strength of the tSZ–CIB correlation. The shaded regions represent the 1σ and 2σ constraints on ξ presented in R12 based on an ℓ-independent correlation template, over the range of angular scales probed by SPT. In this work we also explore the effect, on the derived kSZ power, of using an ℓ-dependent template with a free amplitude, shown by the solid line.

We will explore the dependence of constraints on the kSZ power spectrum on the shape of ξ_ℓ, focusing on the model shown by the solid curve, which has an average correlation coefficient of 0.04, but letting the amplitude freely vary. Note that this is conservative in that models with steeper amplitude have correlations close to zero; however, we will not impose a prior.

5. RESULTS FOR THE OPTICAL DEPTH AND PATCHY kSZ POWER SPECTRUM

In this section, we briefly review the optical depth measurement from WMAP7 in the context of reionization. We then present the SPT patchy kSZ power spectrum measurement, and discuss factors that can affect this result.

5.1. Optical Depth

WMAP measures the optical depth to reionization to be $\tau = 0.088 \pm 0.014$ (Larson et al. 2011). Figure 4 provides intuition on how this constrains the epoch of reionization. In the left panel, we show ionization histories for several models from our simulation database. The right panel plots the large-scale polarization signal as calculated by CAMB (Lewis et al. 2000) from the simulated ionization histories along with the WMAP7 bandpowers. The near instantaneous model at $z_{\mathrm{mid}} = 10.5$ shown by the purple dotted curve, as well as the more extended green dot-dashed curve ($\Delta z \simeq 3$) and very extended blue dashed curve ($\Delta z \simeq 8$) are good fits to the *WMAP* data, as shown in

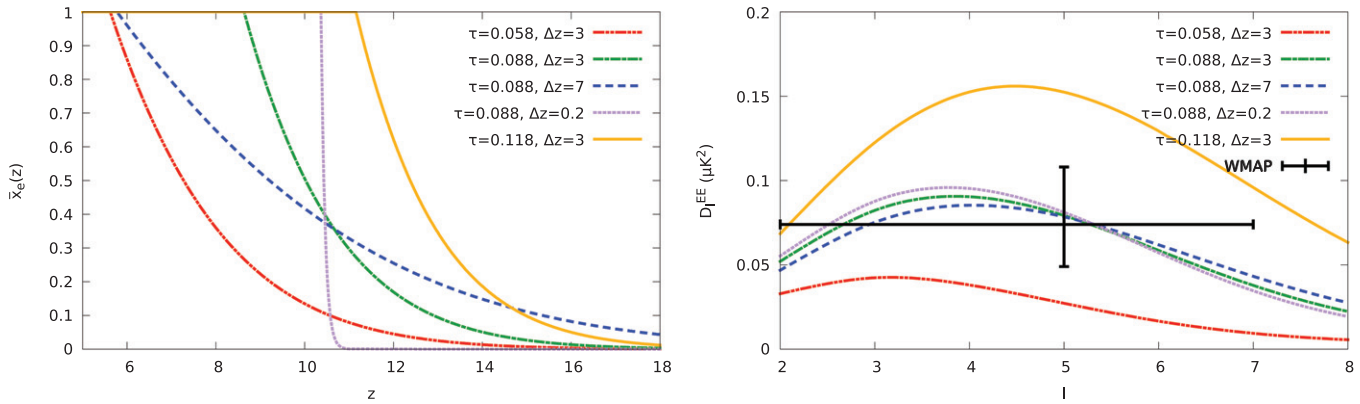

Figure 4. Ionization history and integrated optical depth for different reionization models. The color-coding of model lines is the same between panels. Left panel: evolution of the ionized fraction for each model. Right panel: EE power spectra for the models, together with WMAP7 (Larson et al. 2011) bandpower constraint (black data point). The *WMAP* measurement of *E*-mode power in the band $2 < \ell < 7$ does not restrict the duration of reionization.

(A color version of this figure is available in the online journal.)

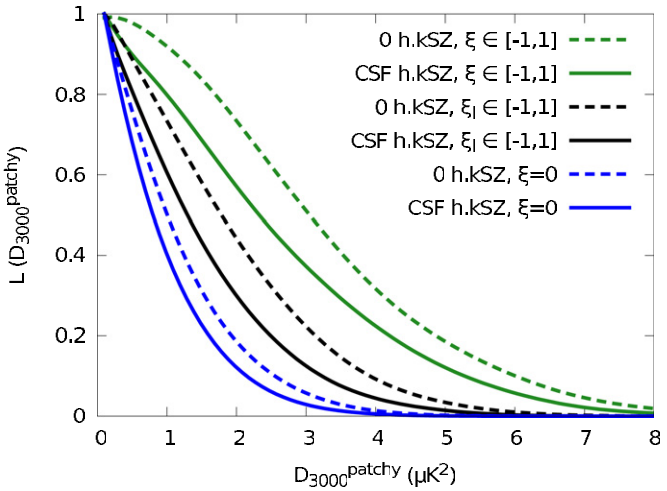

Figure 5. Constraints on the amplitude at $\ell = 3000$ of patchy kSZ fluctuations from the SPT data for different homogeneous kSZ and tSZ–CIB correlation models. The upper limits tighten with the addition of homogeneous kSZ power and with more restrictive assumptions about the tSZ–CIB correlation.

(A color version of this figure is available in the online journal.)

Table 1
kSZ Upper Limits

kSZ Power	$\xi = 0$	$\xi_\ell \in [-1, 1]$	$\xi \in [-1, 1]$
$D_{3000}^{\rm patchy}$ (0 h.kSZ)	2.5 μK^2	3.7 μK^2	5.5 μK^2
$D_{3000}^{\rm patchy}$ (CSF h.kSZ)	2.1 μK^2	3.1 μK^2	4.9 μK^2
$D_{3000}^{\rm kSZ}$	2.7 μK^2	4.1 μK^2	6.1 μK^2

Notes. 95% confidence upper limits on the kSZ power at $\ell = 3000$ for different assumptions about the homogeneous kSZ model and tSZ–CIB correlation, ξ. The first and second rows have limits on the patchy kSZ power assuming either zero homogeneous kSZ power or the CSF homogeneous kSZ model. The third row shows constraints on the total kSZ power for a combined patchy + CSF homogeneous kSZ template. The combined template is used to infer constraints on the epoch of reionization. The first column assumes the most restrictive model for the correlations, $\xi = 0$, and therefore leads to the tightest kSZ limits. The second column allows free correlations with the rising model shape (see Section 4.3 and the solid line in Figure 3) while the third column allows a free, ℓ-independent tSZ–CIB correlation. The latter yields the weakest kSZ upper limits.

the right-hand panel of Figure 4. The large-scale polarization data do not allow one to discern between shorter and longer duration models. However, the red dot-dot-dashed and orange solid curves with $z_{\rm mid} \simeq 7$ and 12.5 are poor fits to the *WMAP* data. For the data used in this paper (CMB+BAO+H_0), the optical depth constraint is $\tau = 0.085 \pm 0.014$. This corresponds to a $\sim$0.25 shift to lower redshifts compared to using the *WMAP*-only optical depth constraint; we use $\tau = 0.085 \pm 0.014$ for all reionization constraints in this work.

5.2. kSZ Power

The SPT constraints on the kSZ power spectrum are summarized in Figure 5 and Table 1. The table contains 95% confidence upper limits on the patchy kSZ power at $\ell = 3000$ for different homogeneous kSZ and CIB models.

The kSZ contributions from various redshifts have the same frequency dependence, and only small differences in angular dependence (as shown in Figure 2). We find that the 2008 and 2009 SPT data presented by R12 do not yet significantly discriminate between the patchy and homogeneous kSZ template shapes. As a result, the modeled homogeneous kSZ power affects the level of patchy kSZ allowed by the data. With more homogeneous kSZ power, less patchy kSZ power is allowed. We note, however, that the patchy kSZ likelihood curves in Figure 5 shift by relatively little when changing the homogeneous kSZ model by $\sim 2\,\mu$K^2. This is because the likelihood curves peak at or below zero kSZ power (-1.2σ without tSZ–CIB correlation), and a positivity prior is applied. As will be discussed below, the SPT data prefer a non-negligible tSZ–CIB anti-correlation together with an increased kSZ amplitude.

We consider two models for the homogeneous kSZ signal. The first, zero homogeneous kSZ (dashed lines in Figure 5), is the most conservative when determining upper limits on the patchy kSZ signal. However, it is physically unmotivated. The second case (solid lines) is the CSF model described in Section 4.1.1 which is our best estimate for the homogeneous kSZ signal. We scale the homogeneous kSZ signal according to the cosmological parameters at each step in the chain following Equation (10). We tabulate the patchy kSZ upper limits with these two homogeneous kSZ models in the first and second rows of Table 1.

To constrain the epoch of reionization, we use kSZ power constraints based on a fixed template set to the sum of the CSF and patchy kSZ models in the fiducial cosmology. Constraints

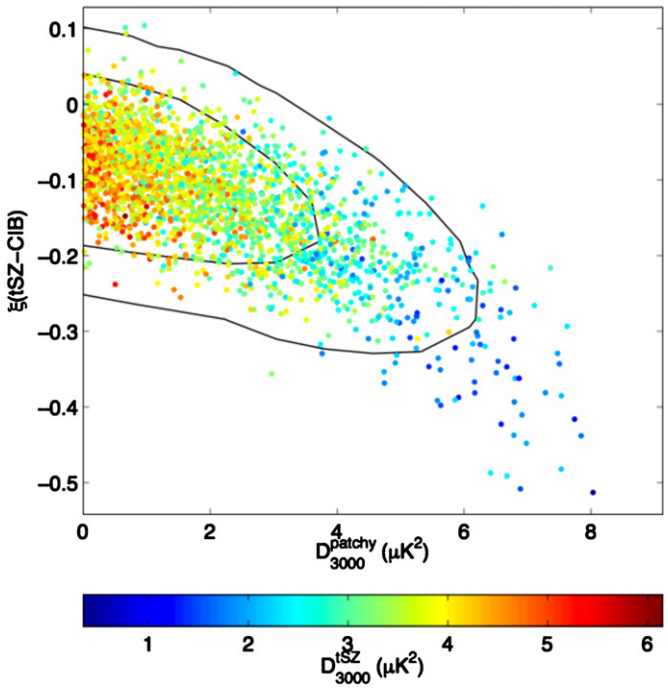

Figure 6. Degeneracy between the patchy kSZ and tSZ–CIB correlation fit to the SPT data. The dots are decorrelated Markov chain samples, color-coded by the tSZ power. The inner/outer contours are 68% and 95% regions, respectively. There is little room for patchy kSZ power with $\xi = 0$. Allowing ξ to be free, the patchy kSZ contribution can be large at the cost of small values of tSZ power.

(A color version of this figure is available in the online journal.)

on the total kSZ power with this template are found in the third row of Table 1. The small error caused by our choice of a fixed ratio between patchy and homogeneous kSZ templates amounts to, at most, a fraction of the observed 15% difference between the kSZ upper limits for the CSF and patchy templates.

A significant uncertainty in the current kSZ constraints is related to the unknown tSZ–CIB correlation. As discussed in Section 4.3, the amount of correlation is highly uncertain; we therefore explore three cases for the correlation. For no correlations, shown by the blue lines of Figure 5 and left column of Table 1, the inferred 95% confidence upper limits on the patchy kSZ power at $\ell = 3000$ are 2.5 and 2.1 μK^2 with the zero and CSF homogeneous kSZ models, respectively. Our second patchy kSZ constraint (black lines in Figure 5 and center column of Table 1) uses a rising tSZ–CIB correlation shape based on the modeling in Section 4.3. This correlation shape is the solid line in Figure 3, and corresponds to the $\xi_{3000} = -0.04$ Shang model case. However, the amplitude of the tSZ–CIB correlation is allowed to vary freely in the MCMC. The third case has an ℓ-independent tSZ–CIB correlation of unknown amplitude. The data prefer a larger anti-correlation in this final case; the 95% confidence range is $\xi_{3000} \in [-0.28, 0.03]$ for the rising correlation shape and $\xi_{3000} \in [-0.43, -0.01]$ for the ℓ-independent correlation shape. As a result, the third case yields the most conservative constraints on the kSZ effect. The 95% confidence upper limits on the patchy kSZ power weaken to 5.5 and 4.9 μK^2 with the zero and CSF homogeneous kSZ models, respectively.

Figure 6 shows the degeneracy between the patchy kSZ contribution, and the tSZ–CIB correlation, ξ. The figure assumes no homogeneous kSZ contribution and an ℓ-independent tSZ–CIB correlation; qualitatively, the result is independent of these assumptions. It is evident that the kSZ power increases with the anti-correlation (more negative values of the correlation, ξ). Anti-correlation has the opposite effect on the tSZ power. The decrease in tSZ power with increasing anti-correlation is shown in the color-coding of the independent samples, ranging from values of 4 μK^2 for the tSZ with zero tSZ–CIB correlation, to small values of 2 μK^2 for a -0.5 correlation.

Decreasing tSZ power with increasing anti-correlation contradicts our naive expectations. In single-frequency bandpowers (e.g., only 150 GHz), increasing tSZ–CIB anti-correlation would increase the allowed tSZ contribution for any observed power level. The anti-correlation term is negative in this band, thereby allowing more tSZ power. However, this picture changes when we consider the SPT multi-frequency data. In Figure 7, we show relevant model components across the three deepest SPT frequency combinations (95 × 150 GHz, 150 × 150 GHz, and 150 × 220 GHz from left to right). We have normalized each model component to 2 μK^2 at 150 GHz and $\ell = 3000$. Note that a tSZ–CIB anti-correlation would lead to a negative power rather than the positive signal (shown by the blue dot-dashed line) in the plot. As shown, a tSZ–CIB anti-correlation reduces the power at 150 × 150 GHz (which could be compensated by increasing tSZ power, shown by the black dashed line) but it also has ∼50% larger effect at 150 × 220 GHz (where there is effectively zero tSZ power). Conversely, a tSZ–CIB anti-correlation reduces the power at 95 × 150 GHz by a similar amount to 150 × 150 GHz, whereas there is more tSZ power in the 95 GHz band. Adding kSZ power (shown as the *combined* template in the black solid line) more effectively compensates for the tSZ–CIB correlation term than adding tSZ power in the most sensitive combinations of the three frequencies. A combination of the kSZ and tSZ does even better, as qualitatively shown by the red dotted line for $1.2D_\ell^{\rm kSZ}$–$0.2D_\ell^{\rm tSZ}$.

6. CONSTRAINTS ON THE EPOCH OF REIONIZATION

In this section, we present constraints on the duration, beginning, and end of reionization. We first interpret the kSZ power in terms of the duration of reionization. We then combine the kSZ constraint from SPT with the integrated optical depth constraint from WMAP7 to constrain the evolution of the ionized fraction as function of redshift, $\bar{x}_e$. Finally, we use the measurement of $\bar{x}_e$ to present limits on $z_{\rm end}$ and $z_{\rm beg}$.

We derive constraints on the history of reionization by comparing the experimental constraints on the total optical depth and the kSZ power to the predicted values for each model in our simulation database. Recall that we use the reionization simulations to predict the patchy kSZ contribution. We then add this patchy power to the power predicted by the CSF homogeneous kSZ model at the fiducial cosmology for the $z_{\rm end}$ of this simulation to estimate the total kSZ power. Uncertainties in the cosmological parameters within the MCMCs used in this paper propagate into a 12.5% uncertainty in the kSZ power spectrum amplitude according to Equation (10). We therefore include a 12.5% Gaussian scatter in $D_{3000}^{\rm kSZ}$ when deriving reionization constraints. This is a good approximation as the kSZ power constraint from the current data is independent of the CMB-derived cosmological parameters.

We marginalize over models in our simulation database, weighting each model by the joint *WMAP*+SPT likelihood. We use a conservative prior of $\bar{x}_e = 1$ at $z \leqslant 5$ based on the model-independent constraints of Fan et al. (2006b) and McGreer et al. (2011).

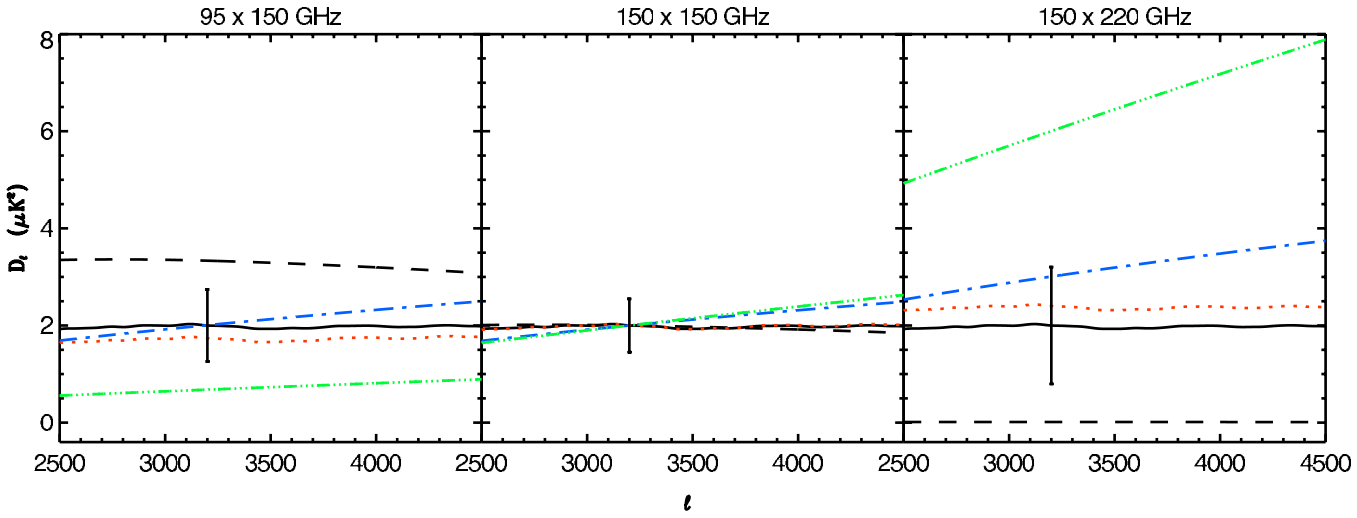

Figure 7. Key model components in the three most important SPT frequency combinations. All model components have been normalized to equal $D_\ell = 2\,\mu\mathrm{K}^2$ at $\ell = 3200$ in the 150 × 150 GHz spectrum. From left to right, the panels show the power spectra for the 95 × 150 GHz, 150 × 150 GHz, 150 × 220 GHz bands. The SPT uncertainty on the average power across the multipole range $\ell \in [2600, 4600]$ is displayed by the black error bars (also centered at $D_\ell = 2\,\mu\mathrm{K}^2$ at $\ell = 3200$). The tSZ–CIB cross power (blue dot-dashed line) increases slightly with frequency, as does a linear combination of tSZ and kSZ (red dotted line). As the tSZ (black dashed line) has the opposite frequency dependence, a tSZ–CIB anti-correlation allows for a larger kSZ amplitude (shown as the combined patchy+homogeneous template in the black solid line). The clustered component of the CIB is shown as well (green dot-dashed line); it has a much steeper frequency scaling.

(A color version of this figure is available in the online journal.)

6.1. Constraints on the Duration of the Epoch of Reionization, $\Delta z_{\rm rei}$

Here we present constraints on the duration of reionization, defined as $\Delta z_{\rm rei} \equiv z_{\bar{x}_e=0.20} - z_{\bar{x}_e=0.99}$. These constraints are primarily due to the SPT kSZ measurement; *WMAP* data alone do not discriminate between reionization models of varying durations. However, by constraining the integrated optical depth, the *WMAP* data indirectly affect the duration inferred from the SPT-derived kSZ constraint since models with given duration have a larger signal at higher redshift due to the higher mean density at higher redshift (see Figure 2).

In Figure 8, we show constraints on Δz for the three tSZ–CIB correlation cases described in Section 5.2. Under the assumption of no tSZ–CIB correlation, we find a 95% upper limit on the duration of $\Delta z < 4.4$. The rising correlation shape template leads to an intermediate limit of $\Delta z < 6.2$. With the ℓ-independent correlation, we find the weakest 95% upper limit of $\Delta z < 7.9$. Note from the left panel of Figure 4 that a shorter redshift interval follows the midpoint of the epoch of reionization than precedes it. As a result, only a fraction of the duration in Figure 8 can lie at lower redshift than the midpoint $z \sim 10.25$.

6.2. Constraints on the Evolution of the Ionized Fraction $\bar{x}_e$

In this section, we show that we can use the CMB data to constrain the history of reionization, $\bar{x}_e$, by combining the constraints on the integrated optical depth and duration of the epoch. To this end, we compute the posterior distributions of $z(\bar{x}_e)$ for all values of $\bar{x}_e$ using our simulation grid given the constraints on τ and the amplitude of the kSZ power spectrum, $D_{3000}^{\rm patchy}$.

As previously mentioned, the integrated optical depth constraint alone cannot constrain the evolution of the ionized fraction as a function of time. Figure 9 shows the 68%/95% confidence intervals in the $z_{\rm end}$–Δz plane. There is a perfect degeneracy in the large-scale *WMAP* polarization data between the duration and end of reionization; a low redshift for the end of

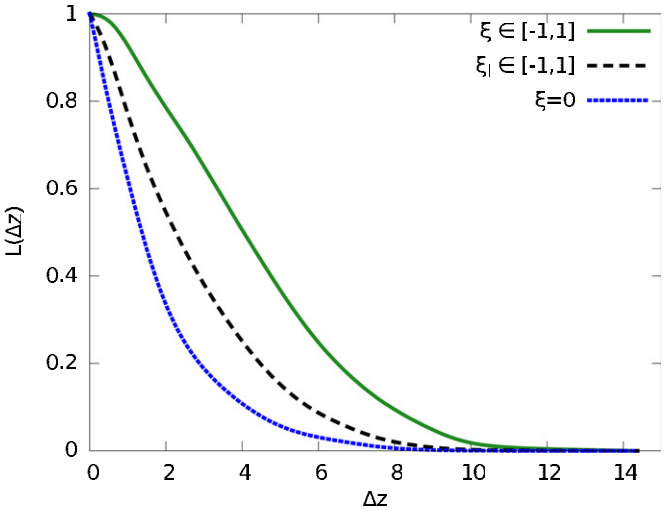

Figure 8. Constraints on the duration of reionization for three assumptions about the tSZ–CIB correlation; free amplitude and scale-independent correlation (solid green line), free amplitude and rising correlation with amplitude consistent with modeling of low correlation simulations (dashed black line); and with correlation set to zero (dotted blue line). We have assumed the CSF homogeneous kSZ model for the post-reionization kSZ signal throughout. The *WMAP* large-scale polarization data enter by constraining the total electron scattering optical depth but are not able to constrain the duration of reionization.

(A color version of this figure is available in the online journal.)

reionization can be made consistent with the data by increasing the duration and the redshift of the starting point of reionization. The SPT constraint on the patchy kSZ contribution breaks this degeneracy by constraining the duration, as shown for the case of no tSZ–CIB correlations in the inner contours of Figure 9.

To obtain constraints on the evolution of the ionized fraction with redshift, we integrate the posterior distributions at each $\bar{x}_e$ to obtain the 68% and 95% likelihood intervals for that ionization fraction to fall within a certain redshift range. Again, we assume the CSF homogeneous kSZ model for the post-reionization kSZ power. As indicated by Table 1, the effect of

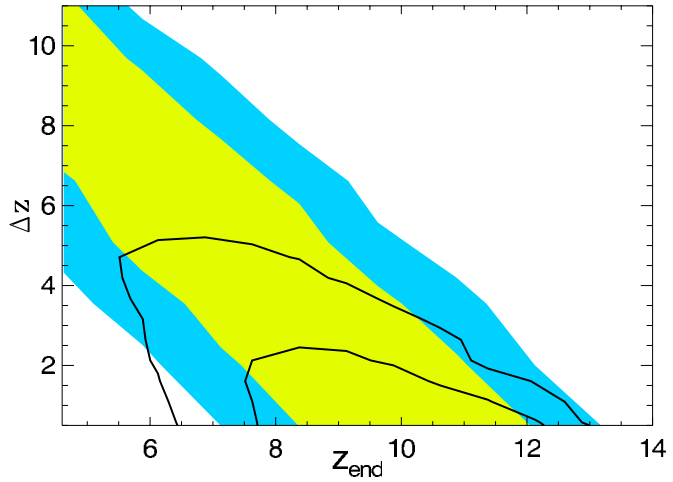

Figure 9. Contour plot of the $z_{\rm end}$–Δz plane showing 68% and 95% confidence regions. There is a degeneracy in the *WMAP* data between the end of reionization and the duration (shaded contours) which is broken by the addition of SPT data (line contours). The tSZ–CIB correlation is assumed to be zero.

(A color version of this figure is available in the online journal.)

Table 2
Reionization Results

		$\xi = 0$	$\xi_\ell \in [-1, 1]$	$\xi \in [-1, 1]$
Δz	(68%)	2.1	2.9	4.4
	(95%)	4.4	6.2	7.9
$z_{\rm beg}$	(68%)	10.7	10.9	11.2
	(95%)	12.1	12.3	13.1
$z_{\rm end}$	(68%)	9.2	8.9	8.3
	(95%)	7.2	6.4	5.8

Notes. Reionization results for different tSZ–CIB correlation assumptions. We have defined volume-weighted ionized fractions of 20% and as the 99% as the beginning $z_{\rm beg}$ and end $z_{\rm end}$ of reionization, respectively, and the duration Δz as the redshift interval between the two. We show 68% and 95% limits in each case as the likelihood surfaces are non-Gaussian. The first two rows (Δz and $z_{\rm beg}$) show upper limits, while the third row ($z_{\rm end}$) shows lower limits. The first column assumes the most restrictive model for the correlations, $\xi = 0$, and therefore leads to the tightest reionization limits. The second column allows free correlations with the rising model shape (see Section 4.3 and the solid line in Figure 3) while the third column allows a free, ℓ-independent tSZ–CIB correlation. The latter leads to the weakest limits on the epoch of reionization.

different homogeneous kSZ power is modest given our tight upper limits. The constraints on $\bar{x}_e$ from the addition of SPT to *WMAP* are shown for the three tSZ–CIB correlation variants in Figure 10. The case with arbitrary, ℓ-independent correlation (right panel, green lines) shows the weakest constraints. The case with rising correlation shape (center panel, black lines) gives intermediate constraints. The case without correlations (left panel, blue lines) shows the tightest constraint on the ionized fraction, with the error on the timing dominated by the *WMAP* optical depth uncertainty. The bulk of the epoch of reionization is confined to a narrow redshift interval from $z \simeq 12.5$ to $z \simeq 7$ at 95% confidence level (CL).

We next consider the end of reionization which has been the focus of most current reionization observations. Recall that we define the end of reionization as $\bar{x}_e = 0.99$. Constraints on $z_{\rm end}$ are shown in the left panel of Figure 11 and tabulated in Table 2. This is equivalent to taking a slice through Figure 10 at $\bar{x}_e = 0.99$. The SPT data enable the first CMB constraint on $z_{\rm end}$. The SPT data disfavor a late end to reionization due to their preference for short durations. For $\xi = 0$, we find that having reionization end at $z_{\rm end} < 7.2$ is disfavored at 95% CL (inner blue contour, dotted line). The constraint weakens considerably when an arbitrary, ℓ-independent correlation is allowed (wider green contour, solid line). However, in this most conservative interpretation of our data, reionization still concluded at $z_{\rm end} > 5.8$ at 95% CL. The rising-ℓ correlation shape yields an intermediate constraint of $z_{\rm end} > 6.4$ (cyan contour, dashed line). Note that while *WMAP* does not place a lower limit on the end of reionization, it trivially places an *upper* limit (the *WMAP* contour lies directly beneath the SPT contours on this side) by limiting the integrated optical depth. Note also that the innermost contour is shifted slightly to the left compared to the cases with tSZ–CIB correlation. This is because the tighter SPT upper limit on the combined kSZ means that short models ending at lower redshift are preferred because they entail a smaller homogeneous kSZ contribution. In other words, there is a slight tension between the SPT requirement for a small kSZ amplitude and the *WMAP* requirement for a relatively large integrated opacity.

Finally, we present constraints on when the first ionizing sources turn on and begin reionizing the universe. Again, we

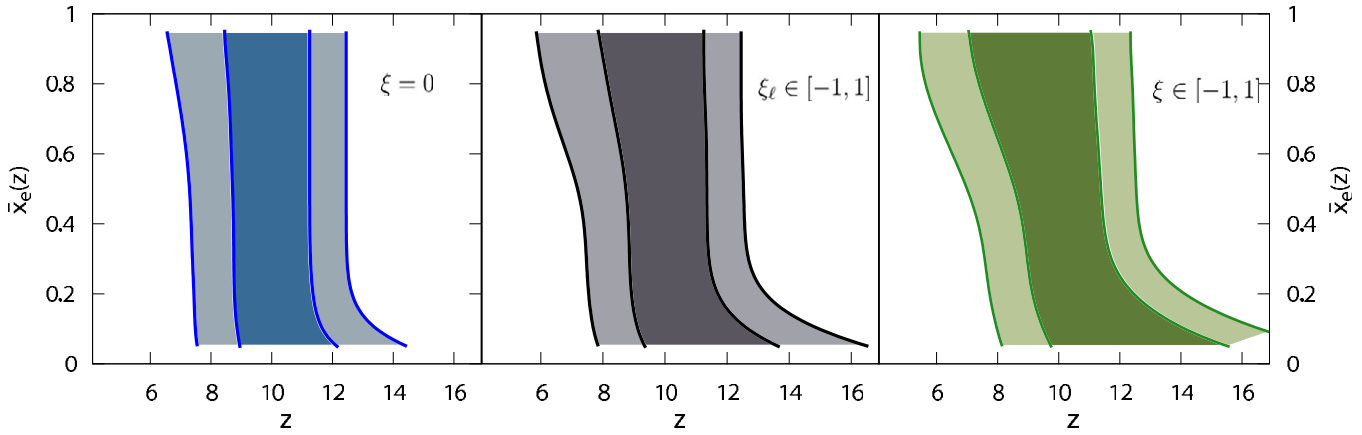

Figure 10. CMB constraints on the evolution of the ionized fraction for three cases of the foreground modeling. The SPT+*WMAP* 68%/95% confidence intervals are indicated by the thick/thin curves. The left panel shows the case without a tSZ–CIB correlation, the center panel shows the free ξ_ℓ case, and the right panel shows the free flat ξ case.

(A color version of this figure is available in the online journal.)

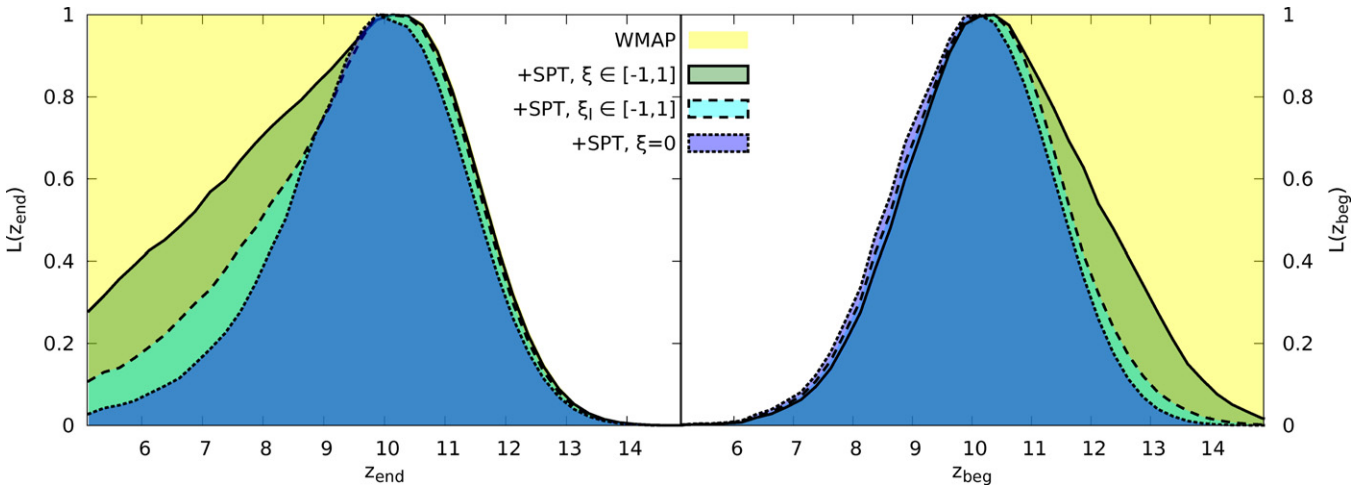

Figure 11. Likelihood functions for $z_{\rm end}$ ($x_e = 0.99$, left panel) and $z_{\rm beg}$ of reionization ($x_e = 0.2$, right panel). In both panels, *WMAP* data only require that the end (beginning) of reionization will be after (before) the midpoint (yellow shading). The most conservative case with SPT data is shown by the green shaded region, solid line. This allows a tSZ–CIB correlation with an ℓ-independent shape. With the cyan region we show results when allowing correlations with the ℓ-dependent shape, dashed line. In the most restrictive case, we neglect correlations (blue shading, dotted line). We have assumed the CSF homogeneous kSZ model for the post-reionization kSZ signal.

(A color version of this figure is available in the online journal.)

have defined the beginning of reionization by $\bar{x}_e = 0.20$. The likelihood function for $z_{\rm beg}$ is shown in the right panel of Figure 11. This is equivalent to taking a slice through Figure 10 at $\bar{x}_e = 0.20$. We find that the combination of *WMAP* and SPT data rule out an early onset of reionization at $z > 12.1$ at 95% confidence in the $\xi = 0$ case. When allowing for a free, ℓ-independent tSZ–CIB correlation, the 95% confidence upper limit increases to $z_{\rm beg} \leqslant 13.1$. Again, the *WMAP* optical depth constraint leads only to a lower limit on the beginning of reionization; see above. Again the $\xi = 0$ likelihood peaks at slightly lower redshift, for the same reason as in the $z_{\rm end}$ case.

6.3. Forecasts for SPT Full Survey, Planck, and Herschel

In the near future, we expect improved measurements of the kSZ power from the full SPT survey, optical depth (from *Planck*), and CIB (from *Herschel* and *Herschel*/SPT cross-correlation analyses). The SPT survey of 2500 deg^2 (three times the area used in this work) was completed in 2011 November. The *Planck* survey is ongoing and the first power spectrum results including the optical depth constraint from the large-scale *E*-mode polarization feature should be released in 2013. *Herschel* observations of the deepest 100 deg^2 of the SPT survey will conclude in 2012, and should enable a detailed study of the tSZ–CIB correlation as well as the CIB in general.

We estimate the improvement in the kSZ power constraint from the full SPT survey with 100 deg^2 of *Herschel* overlap by running an MCMC with simulated bandpowers and uncertainties. We assume a 1% temperature calibration uncertainty and a 5% beam FWHM uncertainty in the SPT frequency bands; we assume that the *Herschel* data are used to create a CIB template map which will be subtracted from the SPT bands to reduce the CIB contribution. Given the wide frequency range spanned, we introduce one new parameter to allow for decorrelation in the CIB between frequency bands. Instead of a single β in Equation (11), we assume a distribution of β in the galaxies of $N(\beta, \sigma_\beta)$. We set a uniform prior of $\sigma_\beta^2 \in [0, 0.35]$; the upper edge is chosen such that the correlation between 150 and 220 GHz is at least 95%. For the full SPT survey without

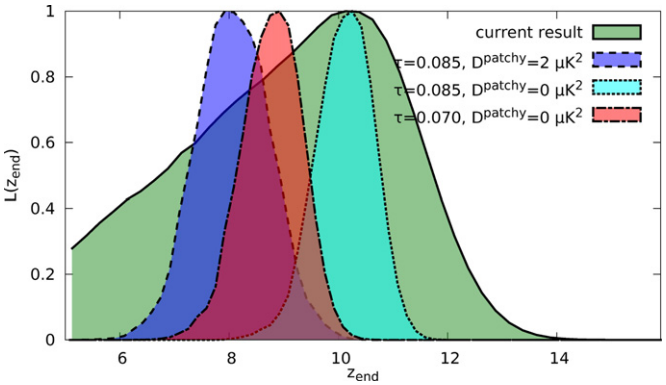

Figure 12. Forecasted $z_{\rm end}$ likelihood functions for future SPT+*Planck*+*Herschel* data. The blue region, dashed line shows the predicted likelihood function assuming zero tSZ–CIB correlation and the median WMAP7 optical depth. We explore the effects of shifting the best-fit values for τ to the WMAP7 lower 1σ bounds in the red region, dot-dashed line, or alternatively of shifting the ℓ-independent tSZ–CIB correlation to the R12 preference of $\xi = -0.18$ in the cyan region, dotted line. The current conservative foreground modeling constraint is shown by the green region, solid line.

(A color version of this figure is available in the online journal.)

Herschel, we find that the kSZ constraint improves proportionally to the reduced SPT bandpower uncertainties; the uncertainties on the bandpowers and kSZ power are reduced by a factor of $\sqrt{3}$. The combination of SPT and *Herschel* leads to a factor of six improvement in the kSZ constraints. Assuming that the post-reionization kSZ contribution is known, we find that the combination of SPT and *Herschel* data should be able to positively identify extended reionization at 95% confidence if $\Delta z \geqslant 2$. Using the *Planck* published sensitivity numbers leads to a forecasted constraint on the optical depth of $\Delta\tau \simeq 0.005$ (Zaldarriaga et al. 2008). This is almost three times better than the current WMAP7+SPT $\tau = 0.085 \pm 0.014$ constraint (Keisler et al. 2011). Figure 12 shows constraint forecasts for the end of reionization. Our current constraints with an uncertain, ℓ-independent, tSZ–CIB correlation is reproduced for comparison in the green contour, solid line. We show three variations on

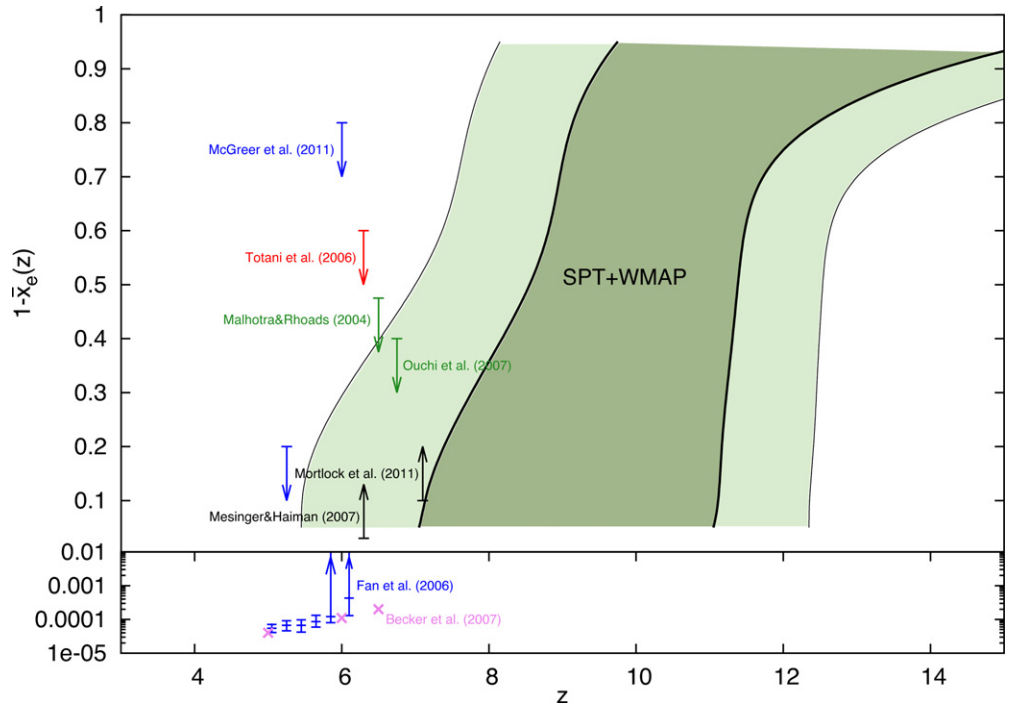

Figure 13. CMB constraint on the redshift evolution of the mean neutral fraction for the (most conservative) free amplitude, ℓ-independent tSZ–CIB correlation case. The SPT+*WMAP* 68%/95% confidence ranges are indicated by the thick/thin curves and the dark/light green shading. We also show other constraints on the neutral fraction based on quasar spectra (blue and violet constraints as well as black lower limits), a gamma-ray burst (red upper limit), and Lyα emitters (green upper limits). (A color version of this figure is available in the online journal.)

the predicted $z_{\rm end}$ likelihood function. The cyan contour (dotted line) shows constraints centered on the WMAP7+SPT optical depth if the combined future data set continues to set only a stricter upper limit on the kSZ power. The predicted $z_{\rm end}$ tightens significantly around $z_{\rm end} \simeq 10.25$ and models that end at $z < 8$ would be ruled out at 95% confidence. At the same τ value, a measured patchy kSZ amplitude of $2\,\mu{\rm K}^2$, corresponding to a reionization duration of $\Delta z \simeq 4$ and in good agreement with the flat correlation at the preferred SPT value of $\xi = -0.18$ leads to the blue contour (dashed line). Reducing the central optical depth to the $\sim 1\sigma$ lower bound of the *WMAP* measurement with zero tSZ–CIB correlation leads to the red contour (dot-dashed line). The latter two cases have similar effects on the $z_{\rm end}$ constraints. The predicted $z_{\rm end}$ tightens around $z_{\rm end} \simeq 8$–8.5 and models that end at $z \lesssim 6.5$ would be disfavored at $\geqslant$95% confidence.

7. DISCUSSION AND CONCLUSION

In this work, we produce the first constraints on the evolution of the ionized fraction during the epoch of reionization using small-scale CMB observations. To this end, we have presented a framework based on efficient reionization simulations to calculate joint constraints on $\bar{x}_e$ from measurements of the total optical depth and kSZ power. We have applied this method to new observations of the kSZ power from the SPT (R12) and published optical depth results from WMAP7 (Komatsu et al. 2011) to probe the beginning, end, and duration of the epoch of reionization.

We find that the SPT kSZ measurement implies a short reionization duration. We show that the SPT kSZ constraint is sensitive to modeling assumptions about the poorly known tSZ–CIB correlation. Assuming this correlation to be negligible leads to the strongest limits on the epoch of reionization duration. Conversely, assuming no outside knowledge of the correlation leads to the most conservative results. The 95% upper limits on the duration are $\Delta z < 4.4$ under the assumption of no correlations and $\Delta z < 7.9$ for the most conservative assumptions. As a result, the SPT data combined with the *WMAP* optical depth constraint rule out reionization models that end very late or begin very early. With ℓ-independent correlations, the epoch of reionization ends at $z > 5.8$ and begins at $z < 13.1$ at 95% CL.

The end of reionization has been the subject of intense theoretical interest and observational effort. In Figure 13, we contrast the most conservative CMB-derived constraint on the *neutral* fraction $1 - \bar{x}_e(z)$ (where $\bar{x}_e \leqslant 1$) with other data. We choose to show $1 - \bar{x}_e$ instead of $\bar{x}_e$ as this is more natural for the other data sets. Specifically, we are allowing an ℓ-independent tSZ–CIB correlation and are assuming the best-guess CSF homogeneous kSZ model for the post-reionization kSZ signal. The dark and light green contours are the 1σ and 2σ likelihood contours, respectively, from the CMB data. Also shown in the upper panel are external constraints on reionization from the Lyα forest (McGreer et al. 2011), LAEs (Malhotra & Rhoads 2004; Ouchi et al. 2010), a gamma-ray burst GRB 050904 (Totani et al. 2006), and quasar proximity regions (Mesinger & Haiman 2007; Mortlock et al. 2011). In the lower panel, we plot constraints on the residual neutral fraction after reionization from the Lyα forest (Fan et al. 2006b; Becker et al. 2007). The previously published data constrain the relatively narrow interval of redshifts $\simeq$5–7. Most results are upper limits, meaning they are consistent with reionization having concluded much earlier. This is also true for the Lyα forest points in the lower panel which correspond to very low neutral fractions (Fan et al. 2006b; Becker et al. 2007). The SPT+WMAP7 data narrows in on a previously unexplored region of the $(z, 1 - \bar{x}_e)$ plane.

Two constraints are in mild tension with our results. These are the *lower limits* on $1 - \bar{x}_e$ obtained from possible detections of damping wing absorption in quasar proximity zones by Mesinger & Haiman (2004, 2007), and to a lesser extent Mortlock et al. (2011) and Bolton et al. (2011). Additional proximity zone spectra, further modeling (e.g., Bolton & Haehnelt 2007a; Maselli et al. 2007; Lidz et al. 2006), and constraints from other data sets should clarify the ionization state of the IGM at $z = 6$–7.

In the future, it would be interesting to investigate whether there is tension with observations of the Lyα forest *after reionization*. In particular, measurements of the mean transmitted flux through the Lyα forest at $z \sim 5$ indicate that the ionizing sources emit only a few ionizing photons per hydrogen atom per Hubble time (Miralda-Escude 2003; Bolton & Haehnelt 2007b). Since after accounting for recombinations a couple of photons per atom are required to complete reionization, these measurements suggest that reionization is a prolonged process.

The results presented here have implications for the proposed study of redshifted 21 cm emission from the hyperfine transition of neutral hydrogen. Observations of the hyperfine transition can potentially provide detailed 3D information about the evolution and morphology of the reionization process (e.g., Zaldarriaga et al. 2004). In the next few years, an ambitious new generation of telescopes will begin collecting data to detect this signal. These efforts include the MWA (Bowman et al. 2005), LOFAR (Harker et al. 2011), GMRT (Pen et al. 2009), PAPER (Parsons et al. 2010), and SKA (Johnston et al. 2008). Improved constraints on the history of reionization can help these experiments select the optimal frequency range in which to focus their observations.

We also note that our results are consistent with the recent result based on the redshifted hydrogen hyperfine transition "global step" experiment EDGES, which produced a lower limit of $\Delta z \geqslant 0.06$ (Bowman & Rogers 2010). Our results are good news for upcoming experiments that hope to detect a redshifted 21 cm absorption feature sourced by substantial UV coupling prior to X-ray heating during the onset of reionization (Pritchard & Loeb 2010; Bowman et al. 2007, 2009; Burns et al. 2011; Harker et al. 2011). The combination of SPT and WMAP7 data limits the early stages of reionization to $z_{\rm beg} \leqslant 13.1$ at the 95% CL, meaning that an ionized fraction of 20% was reached later. While the hyperfine structure absorption feature is expected at somewhat lower ionization fractions, our result indicates that the redshifted 21cm line radiation from this epoch will appear at frequencies higher than those in models with higher $z_{\rm beg}$. There is less galactic synchrotron radiation and radio interference at these higher frequencies.

With a wealth of new data on the horizon, this is an exciting period for CMB reionization constraints. The SPT survey of 6% of the sky is now complete. The kSZ constraints from the full survey should be approximately $\sqrt{3}$ times better than those reported here; kSZ constraints will improve further with the deep SPTpol and ACTpol maps. The *Herschel* satellite is making unprecedented maps of the CIB, including a 100 deg^2 overlap with the deepest 100 deg^2 of the SPT survey. Further submillimeter surveys have started observations or will do so in the near future (e.g., Wootten & Thompson 2009; Radford et al. 2007; Holland et al. 2006). The cross-correlation analysis of *Herschel* and SPT will provide information on the dominant foreground uncertainty for the kSZ power: tSZ–CIB correlations. Finally, the *Planck* survey is ongoing; the first power spectrum results are expected in 2013. The *Planck* data should improve the optical depth constraint by a factor of three. The combination of these data sets should be able to positively identify extended reionization at 95% confidence if $\Delta z \geqslant 2$, further illuminating the epoch of reionization.

We thank Matt George, Guilaine Lagache, Cien Shang, David Spergel, Marco Viero, and Matias Zaldarriaga for useful discussions. The South Pole Telescope is supported by the National Science Foundation through grants ANT-0638937 and ANT-0130612. Partial support is also provided by the NSF Physics Frontier Center grant PHY-0114422 to the Kavli Institute of Cosmological Physics at the University of Chicago, the Kavli Foundation and the Gordon and Betty Moore Foundation. O. Zahn acknowledges support from a Berkeley Center for Cosmological Physics fellowship. The McGill group acknowledges funding from the National Sciences and Engineering Research Council of Canada, Canada Research Chairs program, and the Canadian Institute for Advanced Research. R. Keisler acknowledges support from NASA Hubble Fellowship grant HF-51275.01. B. A. Benson is supported by a KICP Fellowship. M. Dobbs acknowledges support from an Alfred P. Sloan Research Fellowship. L. Shaw acknowledges the support of Yale University and NSF grant AST-1009811. M. Millea and L. Knox acknowledge the support of NSF grant 0709498. This research used resources of the National Energy Research Scientific Computing Center, which is supported by the Office of Science of the U.S. Department of Energy under Contract No. DE-AC02-05CH11231. Some of the results in this paper have been derived using the HEALPix package (Górski et al. 2005). We acknowledge the use of the Legacy Archive for Microwave Background Data Analysis (LAMBDA). Support for LAMBDA is provided by the NASA Office of Space Science. We also acknowledge usage of the FFTW and TeXShop software packages.

REFERENCES

Addison, G. E., Dunkley, J., Hajian, A., et al. 2012, ApJ, 752, 120
Altay, G., Croft, R. A. C., & Pelupessy, I. 2008, MNRAS, 386, 1931
Alvarez, M. A., Busha, M., Abel, T., & Wechsler, R. H. 2009, ApJ, 703, L167
Aubert, D., & Teyssier, R. 2008, MNRAS, 387, 295
Barkana, R., & Loeb, A. 2001, Phys. Rep., 349, 125
Battaglia, N., Bond, J. R., Pfrommer, C., & Sievers, J. L. 2011, arXiv:1109.3711
Becker, G. D., Rauch, M., & Sargent, W. L. W. 2007, ApJ, 662, 72
Bolton, J. S., & Haehnelt, M. G. 2007a, MNRAS, 381, L35
Bolton, J. S., & Haehnelt, M. G. 2007b, MNRAS, 382, 325
Bolton, J. S., Haehnelt, M. G., Warren, S. J., et al. 2011, MNRAS, 419, 2880
Bond, J., Cole, S., Efstathiou, G., & Kaiser, N. 1991, ApJ, 379, 440
Bowman, J. D., Morales, M. F., & Hewitt, J. N. 2005, BAAS, 37, 1217
Bowman, J. D., & Rogers, A. E. E. 2010, Nature, 468, 796
Bowman, J. D., Rogers, A. E. E., & Hewitt, J. N. 2007, ApJ, 676, 1
Bowman, J. D., Rogers, A. E. E., & Hewitt, J. N. 2009, in AIP Conf. Proc. 1035, The Evolution of Galaxies through the Neutral Hydrogen Window, ed. R. Minchin & E. Momjian (Melville, NY: AIP), 87
Bryan, G., & Norman, M. 1998, ApJ, 495, 80
Burns, J. O., Lazio, T. J. W., Bale, S. D., et al. 2011, Adv. Space Res., 49, 433
Cen, R. 2003, ApJ, 591, 12
Choudhury, T. R., Haehnelt, M. G., & Regan, J. 2009, MNRAS, 394, 960
Ciardi, B., Ferrara, A., & White, S. D. M. 2003, MNRAS, 344, L7
Crociani, D., Mesinger, A., Moscardini, L., & Furlanetto, S. 2010, MNRAS, 411, 289
Dwek, E., & Arendt, R. G. 1998, ApJ, 508, L9
Fan, X., Carilli, C. L., & Keating, B. 2006a, ARA&A, 44, 415
Fan, X., Strauss, M. A., Becker, R. H., et al. 2006b, AJ, 132, 117
Finlator, K., Özel, F., & Davé, R. 2009, MNRAS, 393, 1090
Fixsen, D. J., Dwek, E., Mather, J. C., Bennett, C. L., & Shafer, R. A. 1998, ApJ, 508, 123
Furlanetto, S. R., & Oh, S. P. 2005, MNRAS, 363, 1031
Furlanetto, S. R., Zaldarriaga, M., & Hernquist, L. 2004, ApJ, 613, 1
Furlanetto, S. R., Zaldarriaga, M., & Hernquist, L. 2006, MNRAS, 365, 1012

Geil, P. M., & Wyithe, J. S. B. 2008, MNRAS, 386, 1683
George, M. R., Leauthaud, A., Bundy, K., et al. 2011, ApJ, 742, 125
Gnedin, N. Y. 2000, ApJ, 542, 535
Górski, K. M., Hivon, E., Banday, A. J., et al. 2005, ApJ, 622, 759
Gruzinov, A., & Hu, W. 1998, ApJ, 508, 435
Haiman, Z., & Cen, R. 2005, ApJ, 623, 627
Hall, N. R., Knox, L., Reichardt, C. L., et al. 2010, ApJ, 718, 632
Harker, G. J. A., Pritchard, J. R., Burns, J. O., & Bowman, J. D. 2011, MNRAS, 419, 1070
Holland, W., MacIntosh, M., Fairley, A., et al. 2006, Proc. SPIE, 6275, 45
Hultman Kramer, R., Haiman, Z., & Oh, S. P. 2006, ApJ, 649, 570
Iliev, I. T., Mellema, G., Pen, U.-L., et al. 2006, MNRAS, 369, 1625
Iliev, I. T., Mellema, G., Shapiro, P. R., & Pen, U.-L. 2007a, MNRAS, 376, 534
Iliev, I. T., Pen, U.-L., Bond, J. R., Mellema, G., & Shapiro, P. R. 2007b, ApJ, 660, 933
Johnston, S., Taylor, R., Bailes, M., et al. 2008, Exp. Astron., 22, 151
Kashikawa, N., Shimasaku, K., Malkan, M. A., et al. 2006, ApJ, 648, 7
Keisler, R., Reichardt, C. L., Aird, K. A., et al. 2011, ApJ, 743, 28
Knox, L., Scoccimarro, R., & Dodelson, S. 1998, Phys. Rev. Lett., 81, 2004
Kogut, A., Spergel, D. N., Barnes, C., et al. 2003, ApJS, 148, 161
Komatsu, E., Smith, K. M., Dunkley, J., et al. 2011, ApJS, 192, 18
Lagache, G., Puget, J.-L., & Dole, H. 2005, ARA&A, 43, 727
Larson, D., Dunkley, J., Hinshaw, G., et al. 2011, ApJS, 192, 16
Lewis, A., Challinor, A., & Lasenby, A. 2000, ApJ, 538, 473
Lidz, A., McQuinn, M., Zaldarriaga, M., Hernquist, L., & Dutta, S. 2007, ApJ, 670, 39
Lidz, A., Oh, S. P., & Furlanetto, S. R. 2006, ApJ, 639, L47
Malhotra, S., & Rhoads, J. E. 2004, ApJ, 617, L5
Marsden, G., Ade, P. A. R., Bock, J. J., et al. 2009, ApJ, 707, 1729
Maselli, A., Gallerani, S., Ferrara, A., & Choudhury, T. R. 2007, MNRAS, 376, L34
McGreer, I. D., Mesinger, A., & Fan, X. 2011, MNRAS, 415, 3237
McQuinn, M., Furlanetto, S. R., Hernquist, L., Zahn, O., & Zaldarriaga, M. 2005, ApJ, 630, 643
McQuinn, M., Hernquist, L., Zaldarriaga, M., & Dutta, S. 2007a, MNRAS, 381, 75
McQuinn, M., Lidz, A., Zahn, O., et al. 2007b, MNRAS, 377, 1043
McQuinn, M., Lidz, A., Zaldarriaga, M., Hernquist, L., & Dutta, S. 2008, MNRAS, 388, 1101
Mellema, G., Iliev, I. T., Alvarez, M. A., & Shapiro, P. R. 2006, New Astron., 11, 374
Mesinger, A., & Furlanetto, S. 2007, ApJ, 669, 663
Mesinger, A., & Furlanetto, S. R. 2008a, MNRAS, 385, 1348
Mesinger, A., & Furlanetto, S. R. 2008b, MNRAS, 386, 1990
Mesinger, A., & Haiman, Z. 2004, ApJ, 611, L69
Mesinger, A., & Haiman, Z. 2007, ApJ, 660, 923
Mesinger, A., Haiman, Z., & Cen, R. 2004, ApJ, 613, 23
Miralda-Escude, J. 2003, ApJ, 597, 66
Mortlock, D. J., Warren, S. J., Venemans, B. P., et al. 2011, Nature, 474, 616
Oh, S. P., & Furlanetto, S. R. 2005, ApJ, 620, L9
Ostriker, J. P., & Vishniac, E. T. 1986, ApJ, 306, L51
Ouchi, M., Shimasaku, K., Furusawa, H., et al. 2010, ApJ, 723, 869
Page, L., Hinshaw, G., Komatsu, E., et al. 2007, ApJS, 170, 335
Parsons, A. R., Backer, D. C., Bradley, R. F., et al. 2010, AJ, 139, 1468
Pen, U., Chang, T., Hirata, C. M., et al. 2009, MNRAS, 399, 181
Percival, W. J., Reid, B. A., Eisenstein, D. J., et al. 2010, MNRAS, 401, 2148
Petkova, M., & Springel, V. 2009, MNRAS, 396, 1383
Planck Collaboration. 2011, arXiv:1101.2028
Pritchard, J. R., & Loeb, A. 2010, Phys. Rev. D, 82, 023006
Radford, S. J. E., Giovanelli, R., Sebring, T. A., & Zmuidzinas, J. 2007, in Eighteenth International Symposium on Space Terahertz Technology, ed. A. Karpov, 32
Razoumov, A. O., Norman, M. L., Abel, T., & Scott, D. 2002, ApJ, 572, 695
Reichardt, C. L., Shaw, L., Zahn, O., et al. 2012, ApJ, 755, 70
Riess, A. G., Macri, L., Casertano, S., et al. 2011, ApJ, 730, 119
Santos, M. G., Cooray, A., Haiman, Z., Knox, L., & Ma, C. 2003, ApJ, 598, 756
Sehgal, N., Bode, P., Das, S., et al. 2010, ApJ, 709, 920
Semelin, B., Combes, F., & Baek, S. 2007, A&A, 474, 365
Shang, C., Haiman, Z., Knox, L., & Oh, S. P. 2012, MNRAS, 421, 2832
Shaw, L. D., Nagai, D., Bhattacharya, S., & Lau, E. T. 2010, ApJ, 725, 1452
Shaw, L. D., Rudd, D. H., & Nagai, D. 2011, ApJ, in press (arXiv:1109.0553)
Shaw, L. D., Zahn, O., Holder, G. P., & Doré, O. 2009, ApJ, 702, 368
Shin, M.-S., Trac, H., & Cen, R. 2008, ApJ, 681, 756
Sokasian, A., Abel, T., & Hernquist, L. E. 2001, New Astron., 6, 359
Sunyaev, R., & Zel'dovich, Y. 1980, ARA&A, 18, 537
Sunyaev, R. A., & Zel'dovich, Y. B. 1970, Ap&SS, 7, 3
Thomas, R. M., Zaroubi, S., Ciardi, B., et al. 2009, MNRAS, 393, 32
Tinker, J., Kravtsov, A. V., Klypin, A., et al. 2008, ApJ, 688, 709
Totani, T., Kawai, N., Kosugi, G., et al. 2006, PASJ, 58, 485
Trac, H., Bode, P., & Ostriker, J. P. 2011, ApJ, 727, 94
Trac, H., & Cen, R. 2007, ApJ, 671, 1
Trac, H., Cen, R., & Loeb, A. 2008, ApJ, 689, L81
Trac, H., & Gnedin, N. Y. 2009, Adv. Sci. Lett., 4, 228
Wetzel, A. R., & White, M. 2010, MNRAS, 403, 1072
Wootten, A., & Thompson, A. R. 2009, IEEE Proc., 97, 1463
Wyithe, J. S. B., & Cen, R. 2007, ApJ, 659, 890
Wyithe, J. S. B., Loeb, A., & Carilli, C. 2005, ApJ, 628, 575
Zahn, O., Lidz, A., McQuinn, M., et al. 2007, ApJ, 654, 12
Zahn, O., Mesinger, A., McQuinn, M., et al. 2011, MNRAS, 414, 727
Zahn, O., Zaldarriaga, M., Hernquist, L., & McQuinn, M. 2005, ApJ, 630, 657
Zaldarriaga, M., Furlanetto, S. R., & Hernquist, L. 2004, ApJ, 608, 622
Zaldarriaga, M., Colombo, L., Komatsu, E., et al. 2008, arXiv:0811.3918